Fermi National Accelerator Laboratory
P.O. Box 500 - Batavia, Illinois - 60510

Fermilab Engineering Document
NuMI Upgrade AIP Horn-1 Thermal and Structural Analysis
ED0007371, Rev. -

Rev.	Date	Description	Originated By	Checked By	Approved By
-	June 21, 2018	Draft	*Yun He*		

Contents

1. Introduction 2
2. Model and Material Properties 3
3. Cooling Conditions 4
4. Thermal Analysis 5
4.1 Thermal Loads 5
4.1 Temperature at Steady State 7
4.2 Transient Thermal Analysis 10
5. Structural Analysis 13
5.1 Electromagnetic Pressure 13
5.2 Structural Analysis for Steady State, Mid-pulse and End-pulse 14
6. Fatigue Analysis 17
6.1 Evaluation with Von-mises Equivalent Stresses – Methord A 19
6.2 Evaluation with Stress Tensors – Methord B 21
6.3 Comparison of two fatigue evaluation methods 26
6.4 Fatigue Safety Factor Adjustments 27
7. Other Scenarios 27
7.1 Thermal Loading Only at Mid-pulse 27
7.2 Magnetic Loading Only 28
7.3 Current Pulsing Only 28
7.4 Cold startup 30
References 32
Appendix I: Thermal Loads of Horn 1 at Steady State 32

1. Introduction

This report gives a summary of thermo-mechanical analysis of the NuMI Upgrade AIP focusing Horn-1 for operating at a maximum beam power of 1 MW. The Horn-1 is identical to the one currently running at 700 kW for the NOvA beam operations. The 1 MW beam parameters are shown in Table 1.

Table 1: Beam parameters

Proton Beam Energy	Protons / Cycle	Cycle Time	Beam Pulse width	Beam Power	Horn Current/pulse width
120 GeV	6.5E+13	1.2 sec	10μs	1.0 MW	200 kA / 2.3 ms

Horns are coaxial magnetic lenses that focus and direct pions and kaons toward the detectors. The focusing is produced by the toroidal magnetic field present in the air volume between the co-axial inner and outer conductors with a pulsed current, shown in Fig. 1.1.

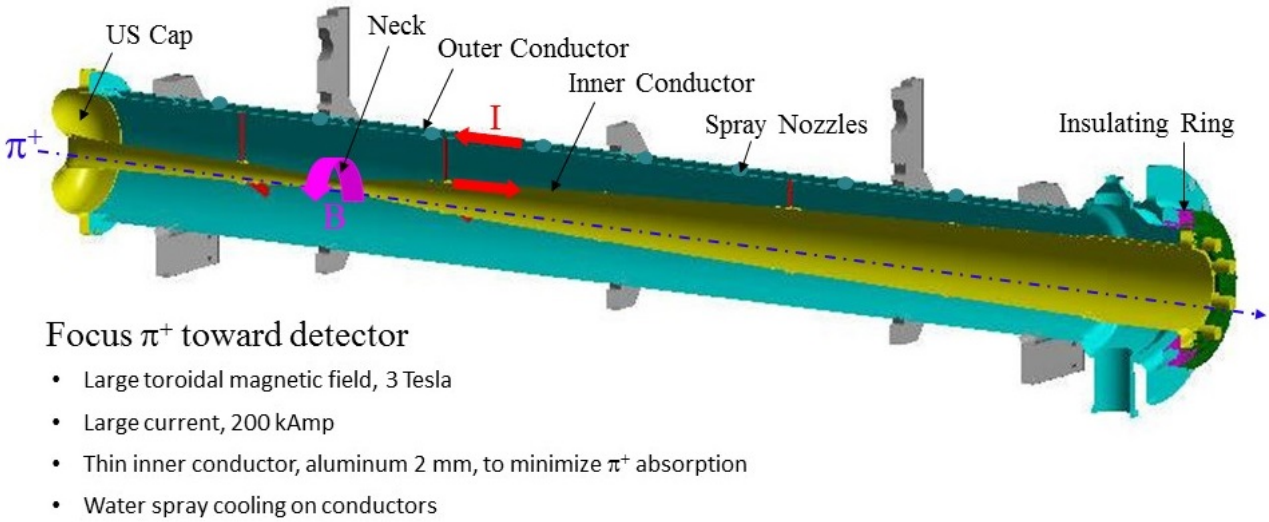

Figure 1.1 Cutaway view of Horn-1

Horn conductors must be able to endure combined thermal loads from electrical resistive heating due to Joule losses and beam heating due to secondary particle interactions with the materials. In addition, current pulsing generates electromagnetic forces on the conductors. Horns are required to withstand repetitive thermal and magnetic loadings over millions of current/beam pulses. Thermal and structural finite element analysis (**FEA**) were carried out with **ANSYS**, and the results are summarized in this report.

The analysis include horn temperature, deformation and stress studies for steady state, immediately after beam, and immediately after current pulse in nominal operation conditions, current pulsing only, beam only, and cold start. The horn fatigue strength for 10^8 cycles is evaluated.

2. Model and Material Properties

The FEA model includes a complete assembly of the outer conductor (O.C.) and inner conductor (I.C.), made of Aluminum 6061. They are connected with an Alumina ceramic insulating ring. Three sets of Aluminum thin strips represent the radial spider supports of the I.C. The thermal load calculations are given for the model sliced into about 168 segments in axial direction, shown in Fig. 2.1, with an assumption of uniform heating load density in each segment. Fig. 2.2 shows the mesh of the Horn 1 FEA model. The material properties are listed in Table 2.1.

Figure 2.1: FEA model of Horn-1

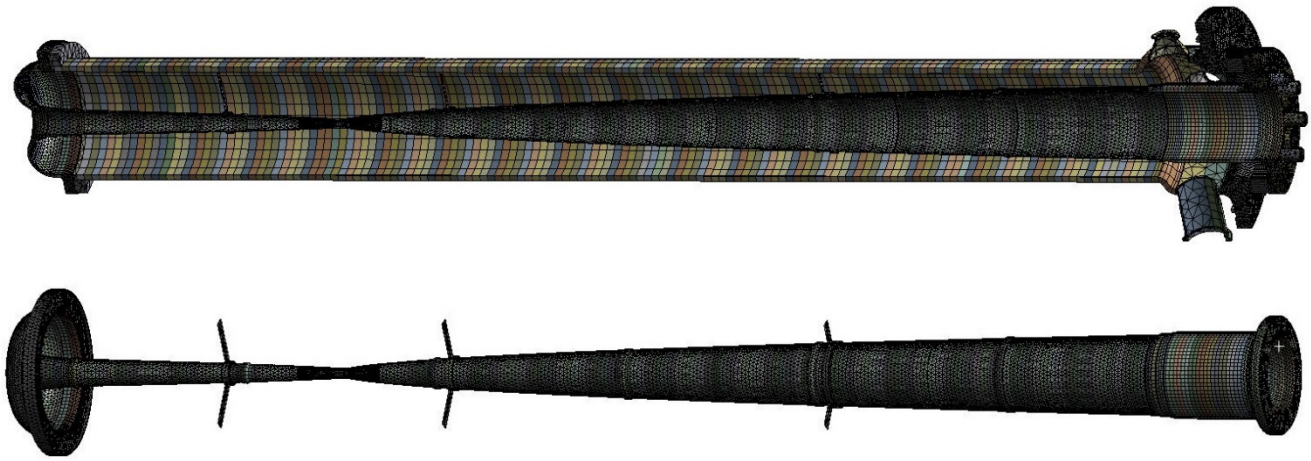

Figure 2.2: Mesh of Horn1 FEA model

Table 2.1: Material properties [1]

Structural	Aluminum 6061 T6	99.8% Alumina Ceramic
Young's Modulus, GPa	68.9	370
Poisson's Ratio	0.33	0.22
Density, kg/m³	2700	3920
Thermal Expansion, 10^{-6} 1/°C	23.6	8.2
Tensile Yield Strength, MPa	276	
Tensile Ultimate Strength, MPa	310	248
Compressive Strength, MPa		2500
Thermal		
Thermal Conductivity, W/m·°C	167	30
Specific Heat, J/kg·°C	896	880

3. Cooling Conditions

The horn conductors are cooled with closed loop radioactive water (RAW) and air in the chase. The outer surfaces of I.C. are cooled by spraying water, with spray nozzles distributed along the beam axis and 120° azimuthally. Spray nozzles on the top of the O.C. cylinder spray water to form a film running down from both sides of the wall, shown in Fig.3.1. The inlet water temperature is 21ºC.

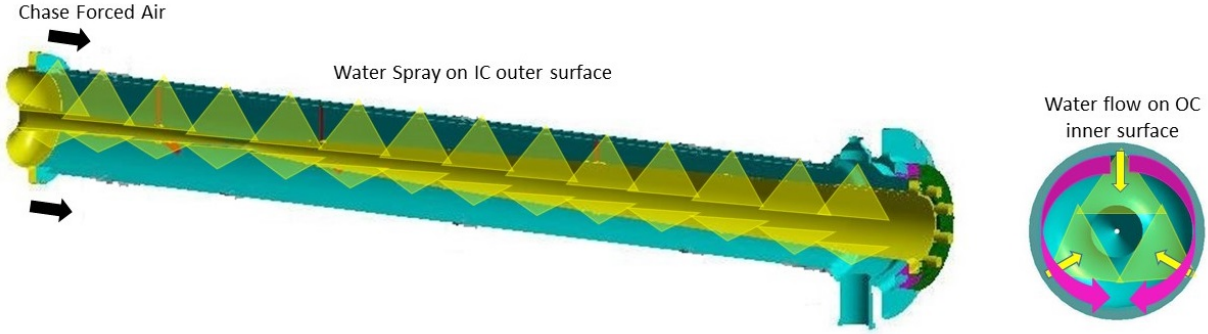

Figure 3.1: Horn cooling conditions

The heat transfer coefficients of water cooling were obtained through experiments. For the I.C. outer surfaces, the values are varied along the length of horn, depending on the effective area coverage of the water spray [2][3]. With a RAW cumulative flow increase from ~35 gpm to ~45 gpm, the heat transfer coefficients are increased compared to those for the NOvA operation, shown in Table 3.1 and Fig. 3.2,

Table 3.1: Convective heat transfer coefficient for I.C. external surfaces

Distance from upstream CAP	Heat Transfer Coefficient (W/m2-K) for AIP	Heat Transfer Coefficient (W/m2-K) for NOvA
0-50cm	4800	3900
50cm-110cm	6500	5000
110cm-290cm	3550	2750
290cm-330cm	6500	2120

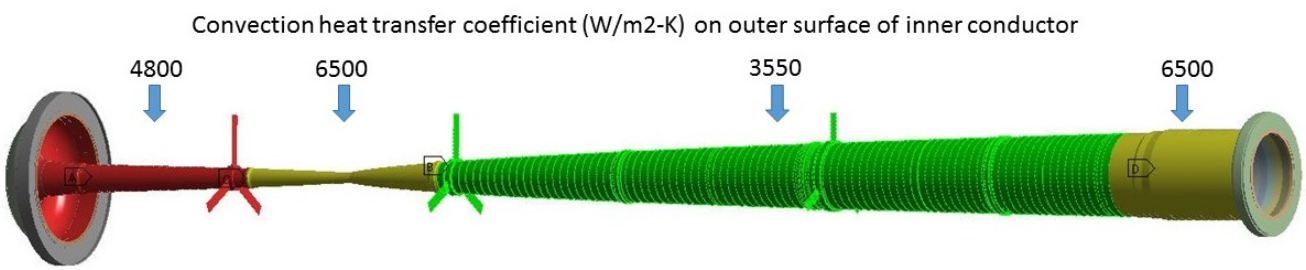

Figure 3.2: Heat transfer coefficients defined in the Horn 1 FEA model

For the O.C. inner surfaces, the value is estimated to be 1500 W/m^2-K. The exterior surfaces of Horn are exposed to chase air with a 25 °C inlet temperature. It is assumed that the heat transfer coefficient of air is 10 W/m^2-K for the O.C. external surfaces which are exposed to the chase forced air, and 5 W/m^2-K for the I.C. bore external surfaces which are sheltered from the chase airflow. On the downstream (DS) flange, there is a water cooling clamp. With a Φ0.375 channel and a 1.6 gpm flow rate, the heat transfer coefficient is estimated to be 6950 W/m^2-K [4].

Table 3.2: Convective heat transfer coefficient for other surfaces

	Heat Transfer Coefficient (W/m^2-K)	Temperature
Outer conductor internal surface	1500	21 °C
Outer conductor external surface	10	25 °C
Inner conductor bore external surface	5	25 °C
DS flange cooling clamp channel	6950	21 °C

4. Thermal Analysis

4.1 Thermal Loads

The heating on Horn conductors come from three sources:

1) Electrical resistive heating due to Joule losses;
2) Beam heating due to secondary particle interactions with the materials;
3) Thermal radiation from surrounding shielding blocks.

At this time, the temperature evaluation of the radiation blocks is not available, and this 3rd thermal load is expected to be only 10% of the other two heating sources. Therefore it is ignored in this study.

The horn current pulse is a half-sine wave with a peak current of I = 200 kA, pulse width of t = 2.3 ms, and a repetition rate of T = 1.2 s.

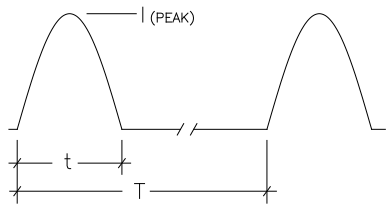

$$Irms = \mathrm{I(peak)}\sqrt{\frac{t}{2T}}$$

The skin depth (the depth below the surface at which the current density decays to 1/e of the current density at the surface) of the pulsed current can be calculated as follow:

$$\delta = \sqrt{\frac{2\sigma}{\omega\mu}} = 6.8 \text{ mm}$$

Where, σ = resistivity of conductor; ω = angular frequency of current, $\omega t = \pi$, μ = absolute magnetic permeability of conductor, 1.256 x 10^{-6} (H/m). The wall thickness of Horn-1 inner conductor is 2 mm, therefore the skin effect can be neglected that all the charge are assumed to be distributed uniformly across the wall thickness.

The beam energy deposition (ED) rates (GeV/cm^3-proton) in the Horn conductors are obtained from MARS simulations [5], for the target condition of a 9 mm NOvA target fin width with a 1.5 mm beam sigma. The data are given for the model sliced into 2cm-long segments in axial direction, shown in Fig. 4.1.

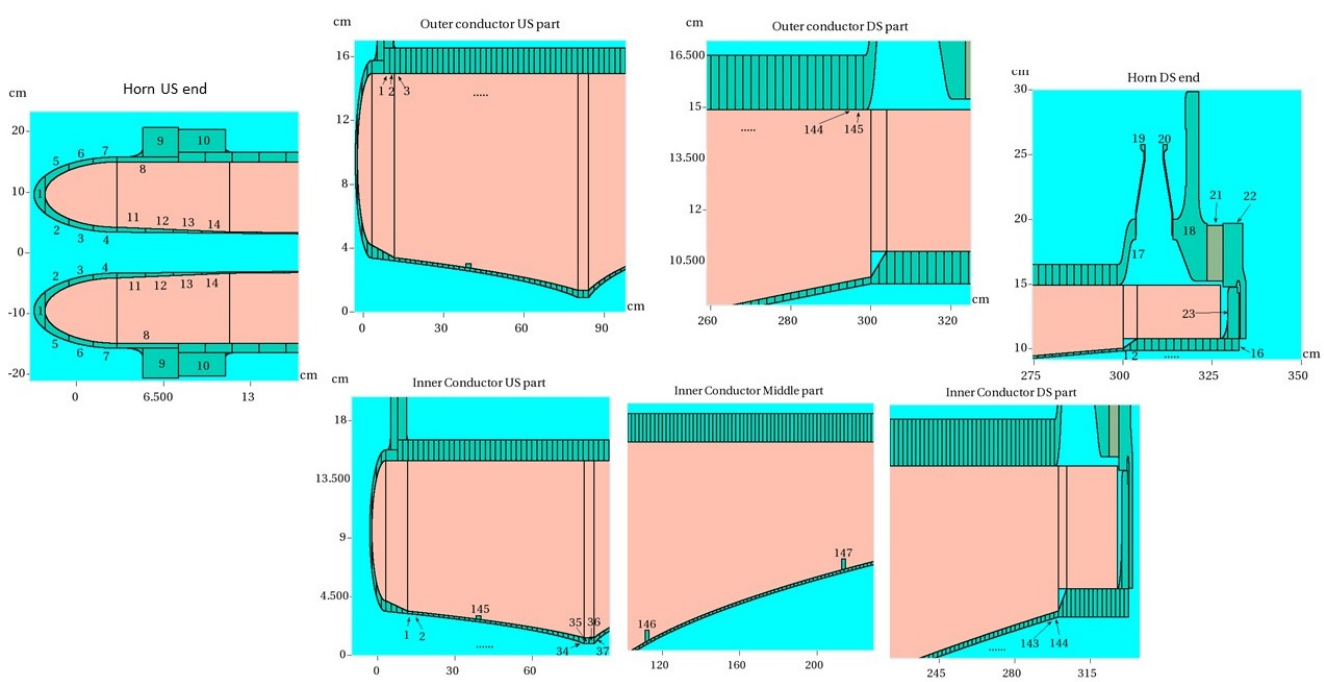

Figure 4.1: MARS map of Horn 1 with 2cm-long sliced bins

4.1 Temperature at Steady State

We started the analysis with steady state thermal analysis first, assuming the hating loads per pulse are uniformly input in 1.2s, the current pulse/beam spill cycle time.

The electrical resistive heating is calculated with the following formula:

$$P_j = \frac{\sigma_T * I^2 * t}{2A^2\ T}$$

Where, A is cross-sectional area of I.C.. The resistivity σ_T changes with temperature and is expressed as:

$$\sigma_T = \sigma_0 * [1 + a * (T - T_0)]$$

Where, σ_0 = 3.99 x 10^{-6} ohm-cm for Al 6061-T6, resistivity at reference temperature; a = 3.8 x 10^{-3}, temperature coefficient of resistivity (1/°C); T_0 = 25 °C, reference temperature.

The MARS ED outputs are expressed in GeV/cm^3 per proton. They are converted into average beam heating power density in W/cm^3 for load input in the FEA model with the ratio below:

$$\text{ratio} = \frac{(1.60217646E-10)*(6.5E+13)}{1.2}$$

Fig. 4.2 and Fig. 4.3 provide the plot of the thermal load density in each 2-cm segment along the Horn axial location for I.C. and O.C., respectively. The maximum heating load density is 37 W/cm^3, located on the Neck. The Joule heating on O.C. is negligible, compared to the beam heating.

The tabular thermal loads data with Horn geometrical values are listed in Appendix I-a.

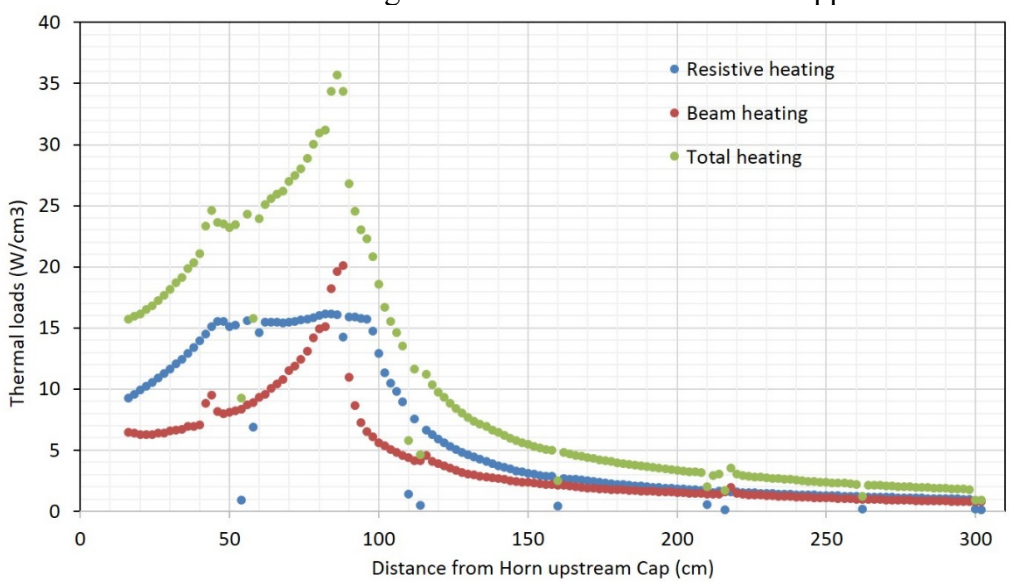

Figure 4.2: Thermal loads on Horn 1 inner conductor

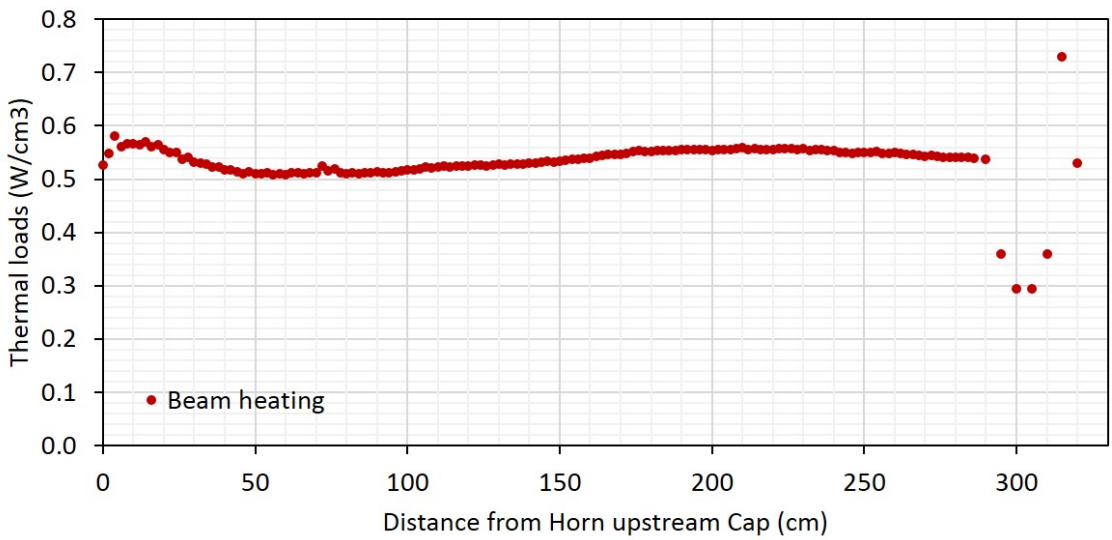

Figure 4.3: Thermal loads on Horn 1 outer conductor

The summary of the thermal loads is listed in Table 4.1.

Table 4.1: Thermal Loads on Horn-1 (kW)

	I.C.	O.C.	Ceramic Ring	End Flange
Beam Heating Loads	12.6	32.6	1.52	1.48
Joule Heating Loads	8.4			

The calculated temperatures are shown in Fig. 4.4. The maximum temperature would be 43°C on the I.C. Neck, and 52.7°C on the downstream flange.

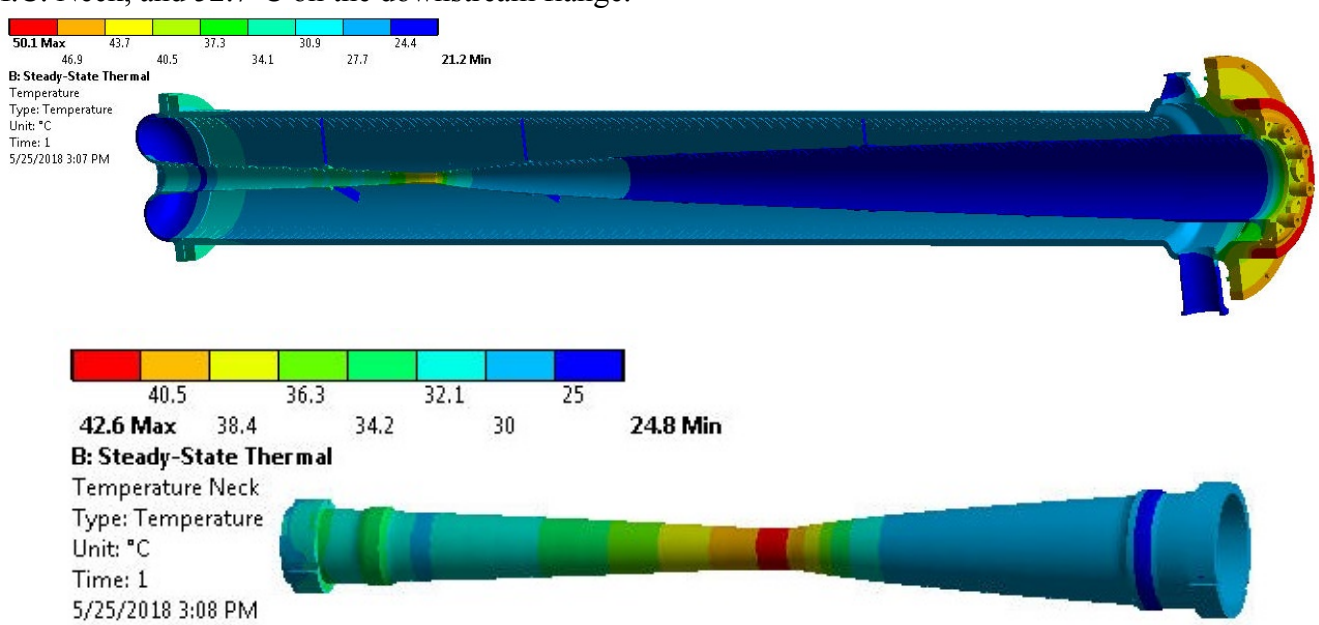

Figure 4.4: Temperature at steady state

It will take about 9.6 seconds or 8 beam pulses to reach this equilibrium temperature, shown in Fig. 4.5.

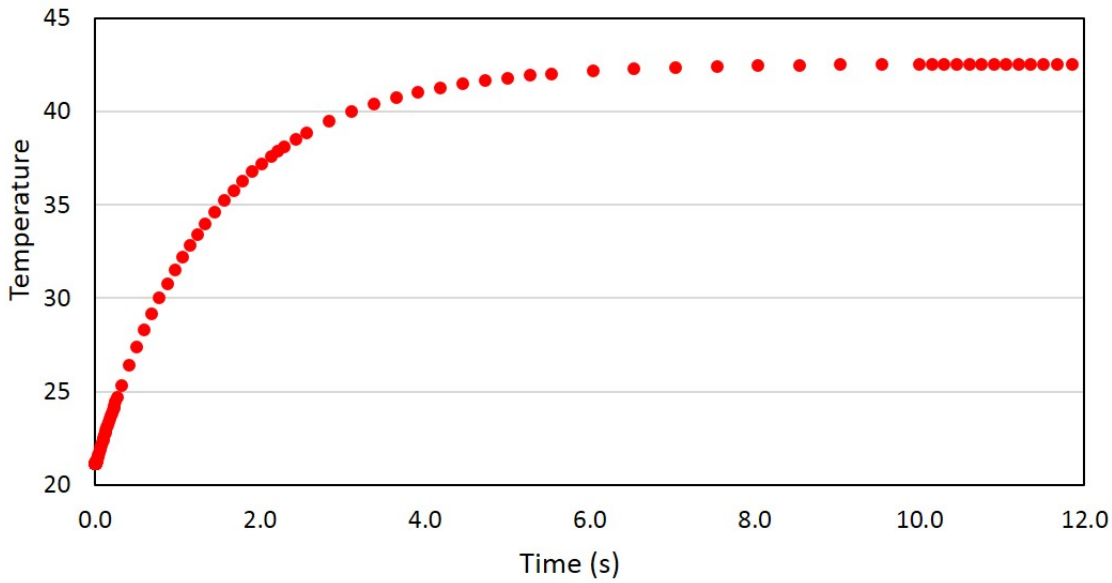

Figure 4.5: Neck temperature trend from cold startup to equilibrium

Now we use analytical calculation to check the validation of the FEA temperature results.

Let us exam a single bin on the Neck of Horn-1 located at Z = 86 cm, where it receives a peak heating load density. It is 2 cm long, with an outer radius of 1.325 cm and thickness of 0.45 cm. We will refer this segment as **Neck** in the following analysis.

The heating loads on this bin Q = 227 W, shown on the third row in Table 4.2.

Table 4.2: Heating loads on Horn-1, a section extracted from Table I-a:

Bin No.	Z	Volume	Thickness	Outer-radius	Resistive Heating		Beam Heating			Total heating
	cm	cm³	cm	cm	W/cm³	W	GeV/cm³-proton)	W/cm³	W	W/cm³
35	84	6.36	0.45	1.35	16.15	102.7	2.10E-03	18.21	115.8	34.36
36	**86**	**6.35**	**0.45**	**1.35**	**16.09**	**102.2**	**2.26E-03**	**19.60**	**124.6**	**35.70**
37	88	6.23	0.37	1.64	14.24	88.7	2.32E-03	20.10	125.2	34.34
38	90	6.43	0.29	1.90	15.87	102.1	1.26E-03	10.93	70.4	26.81

With a convective heat transfer coefficient of h = 6500 W/m^2-C, temperature rise on the outer surface of this bin can be calculated with the formula:

$$\Delta T = \frac{Q}{hA} = 20.5\ °C$$

Plus the water input temperature 21°C, that gives a Neck temperature of 42°C, which has a good agreement with the FEA results shown in Fig. 4.4.

Table 4.3: Convective heat transferred loads

	Heat Transfer Coefficient (W/m^2-K)	Removed (W)
0-50cm	4800	5988.6
50cm-110cm	6500	4320
110cm-290cm	3550	6193.3
290cm-330cm	6500	4256.5
Outer conductor internal surface	1500	29487
Outer conductor external surface	10	124.2
Inner conductor bore external surface	5	40.1
DS flange cooling clamp channel	6950	1111.5

4.2 Transient Thermal Analysis

Transient thermal analysis was carried out for a single pulse. The current pulse is shown in the Fig. 4.6. The pulse width is 2.3 ms.

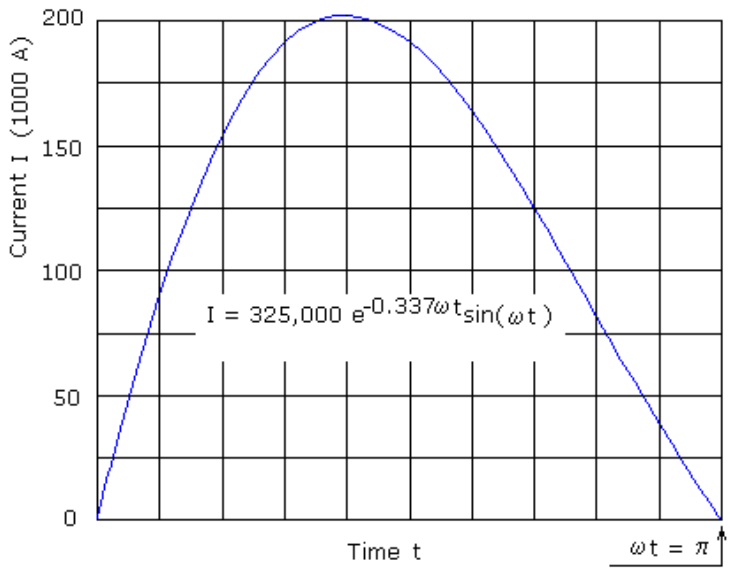

Figure 4.6: Current pulse

We divide the 2.3 ms into 10 steps, and take the average joule heating load in each 0.23 ms period. At the middle of the current pulse, at 0.91 ms, beam is on for 10 μs. The thermal load is the sum of the joule heating and the beam heating, shown in Fig. 4.7.

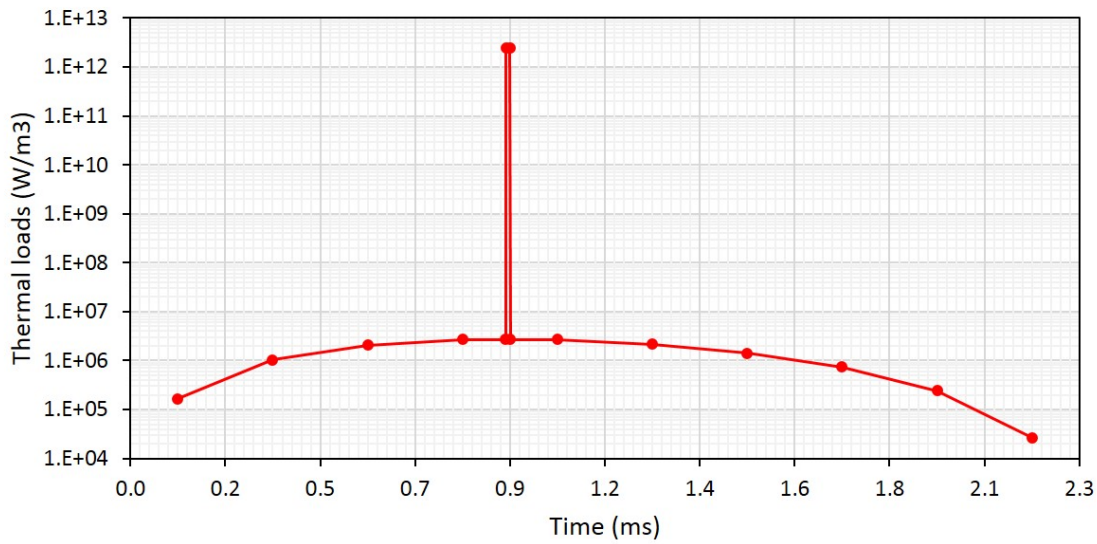

Figure 4.7 Thermal loads on Neck during a single pulse

During each current/beam pulse the temperature on the Neck will rise by 11°C, shown in Fig. 4.8.

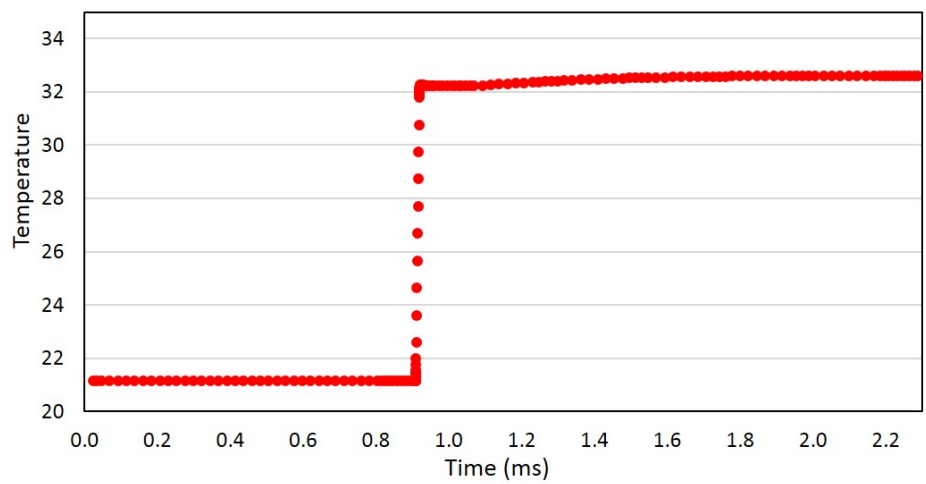

Figure 4.8: Neck temperature trend during a single current/beam pulse from cold startup

After reaching the equilibrium temperature, during each current/beam pulse the temperature on the Neck will rise from 42.6°C to 54°C, shown in Fig. 4.9. The temperature would then gradually return to the equilibrium before the next pulse.

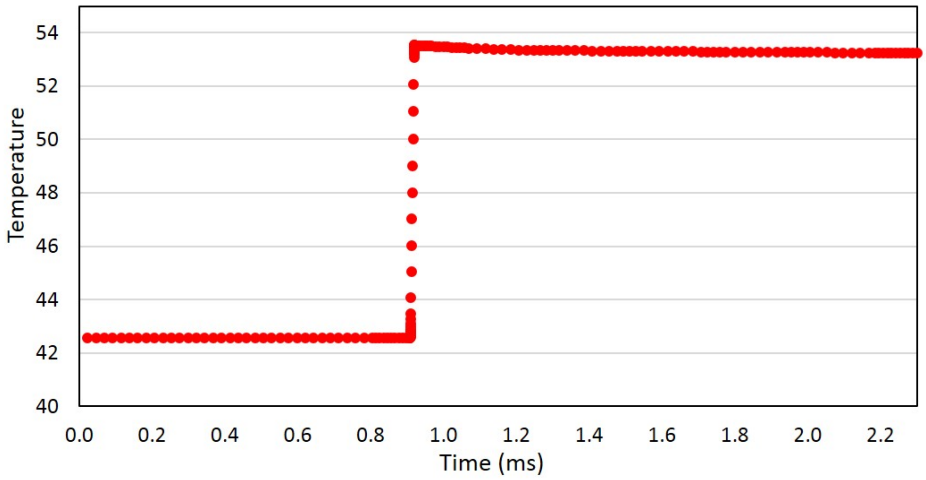

Figure 4.9: Neck temperature trend during a single current/beam pulse after equilibrium

Temperatures profile at beam-end at 0.921ms (Mid-pulse) and current-pulse-end at 2.3 ms (End-pulse) are shown in Fig.4.10.

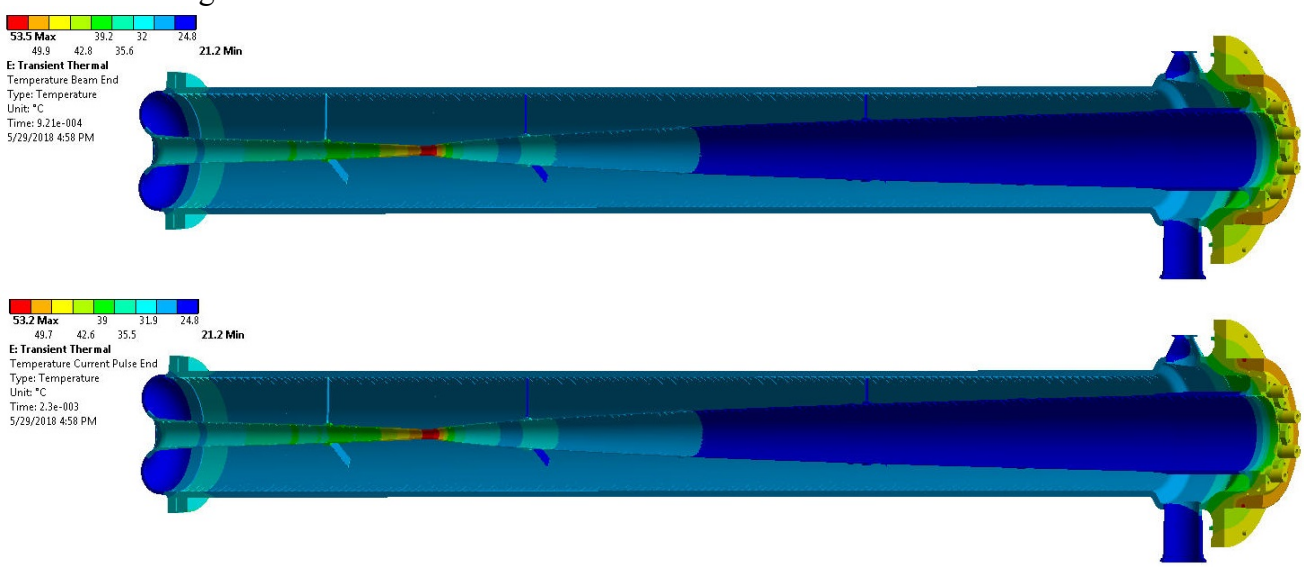

Figure 4.10: Temperature distribution at Mid-pulse (upper) and End-pulse (lower)

The temperature rise on most parts beyond the central section is less than 5°C, shown in Fig. 4.11.

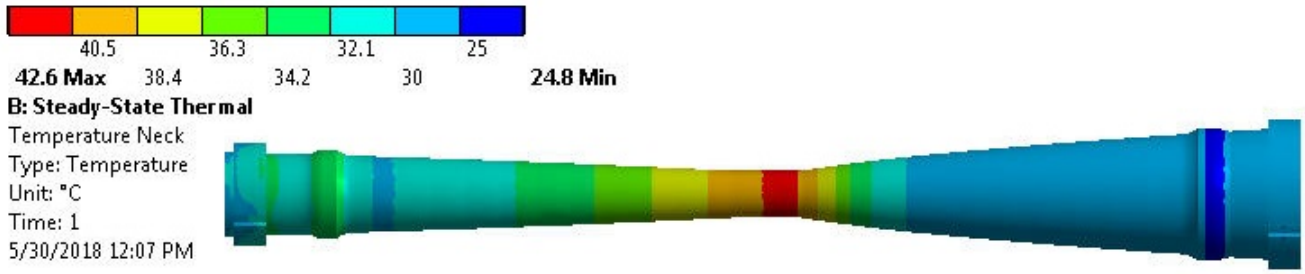

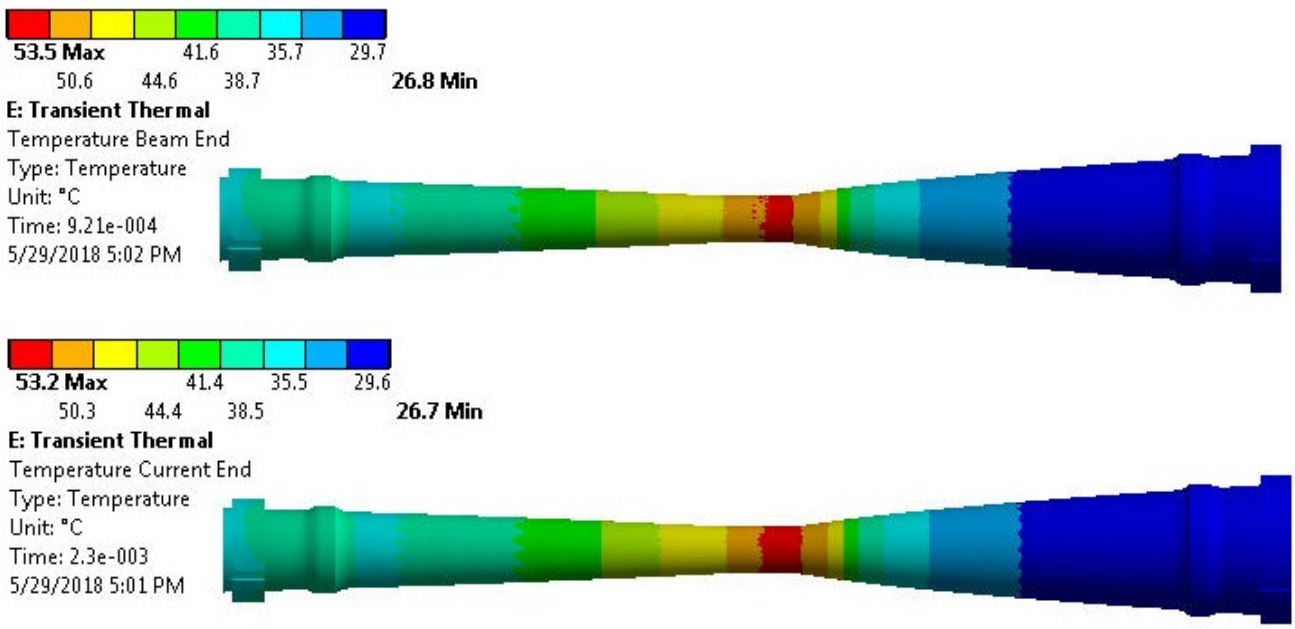

Figure 4.11: Horn-1 central section temperatures at steady state, mid-pulse and end-pulse

Now we use analytical calculation to check the validation of the FEA temperature results. Let us exam the single bin on the Neck of Horn-1 located at Z = 86 cm. With a beam heating power density of Q = 35.6 W/cm^3 = 42.72 J/cm^2 and a specific heat of c = 896 J/kg-C of Aluminum, a volume of 6.22 cm^3, the instantaneous temperature jump on this bin can be calculated to be 7.6°C:

$$\Delta T = \frac{Q}{m\,c} = 7.6°\text{C}$$

5. Structural Analysis

Static structural calculations were performed to study the stresses at steady state, mid-pulse and end-pulse. The temperature solution from thermal analysis was loaded as thermal loading. The boundary conditions in the structural environment were set as free thermal expansions, which are to be accommodated by the Horn support structure involving pivot system. Horn gravity was applied.

For the mid-pulse state, at peak current immediately after beam spill, magnetic pressure was applied in addition to the thermal loading. For the steady state and end-pulse state, only thermal loading was applied.

5.1 Electromagnetic Pressure

The pulsed current running on horn produces the B-field in the air cavity enclosed by the I.C. and O.C.. The B-field interacts with the pulsed current and yields electromagnetic forces on the conductors:

$$f = \mathbf{j} \times \mathbf{B} = \frac{\mu_0 I^2 x}{4\pi^2 R^2 t^2}.$$

Integrate the force through the thickness, we obtain pressure perpendicular to the horn surface:

$$p = \frac{\mu_0 I^2}{8\pi^2 R^2}. \qquad (5.1)$$

The electromagnetic pressures as a function of the Horn axial locations are shown in Fig. 5.1. The maximum magnetic pressure of 3.5 MPa will occur on the neck pointing inward. The pressure decomposes into an axial component, owing to the Horn's parabolic character, contributing tensile stresses to the transition from tube to end caps.

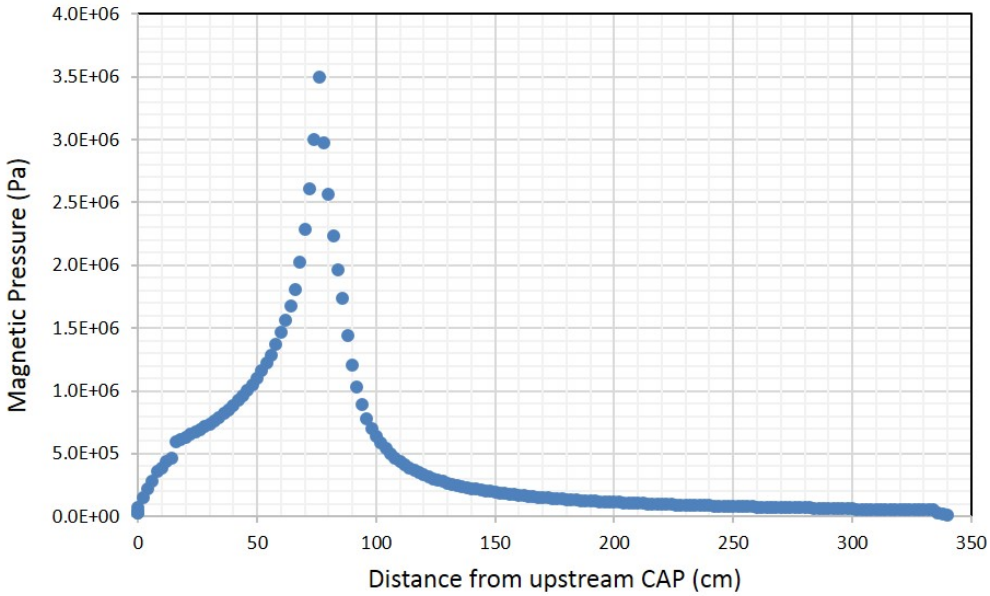

Figure 5.1: Magnetic pressure on Horn1 IC at peak current

5.2 Structural Analysis for Steady State, Mid-pulse and End-pulse

Mechanical stresses were calculated for steady state, Mid-pulse and End-pulse. The temperature solution from thermal analysis was loaded as thermal loading. For the Mid-pulse case, magnetic pressure was applied in addition to the thermal loading. The earth gravity is applied.

The stress distributions are shown in Fig. 5.2-5.3. The equivalent stresses on most part of Horn are below 15 MPa, except three locations, US cap, Neck, and DS ceramic ring shown in Fig. 5.4.

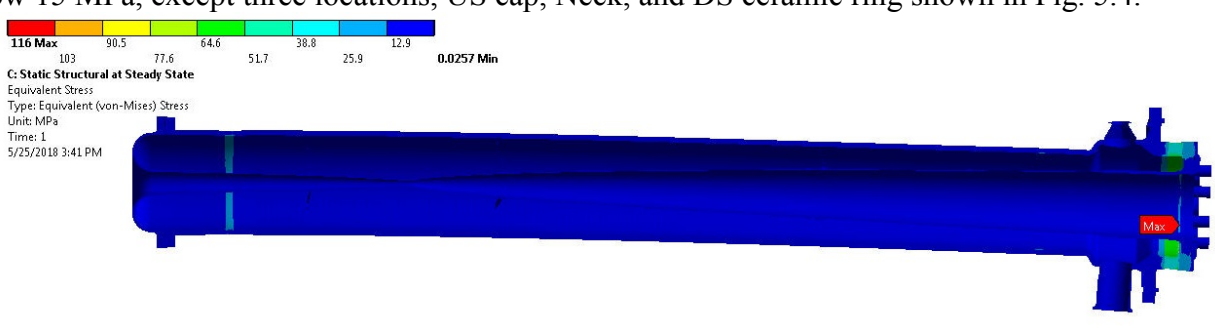

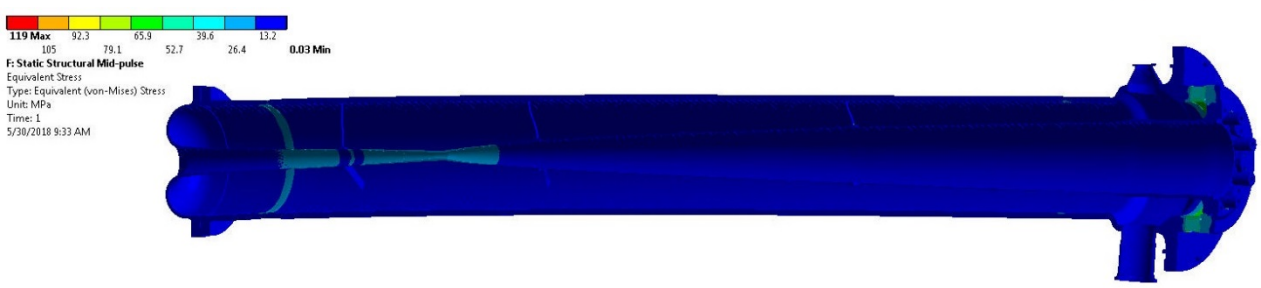

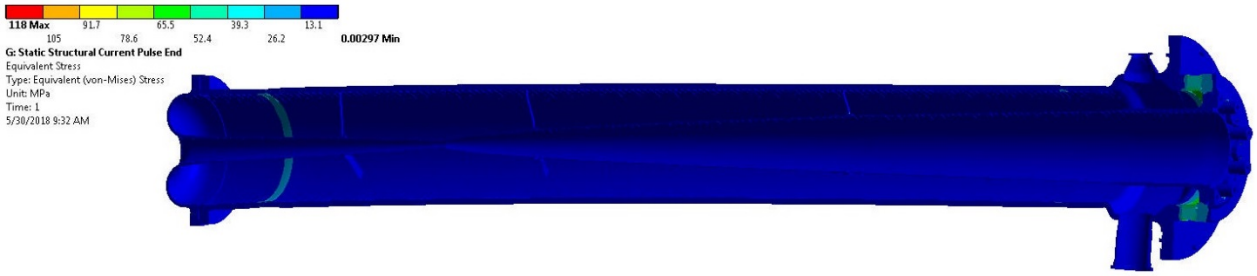

Figure 5.2: Horn1 stresses at steady state, mid-pulse and end-pulse

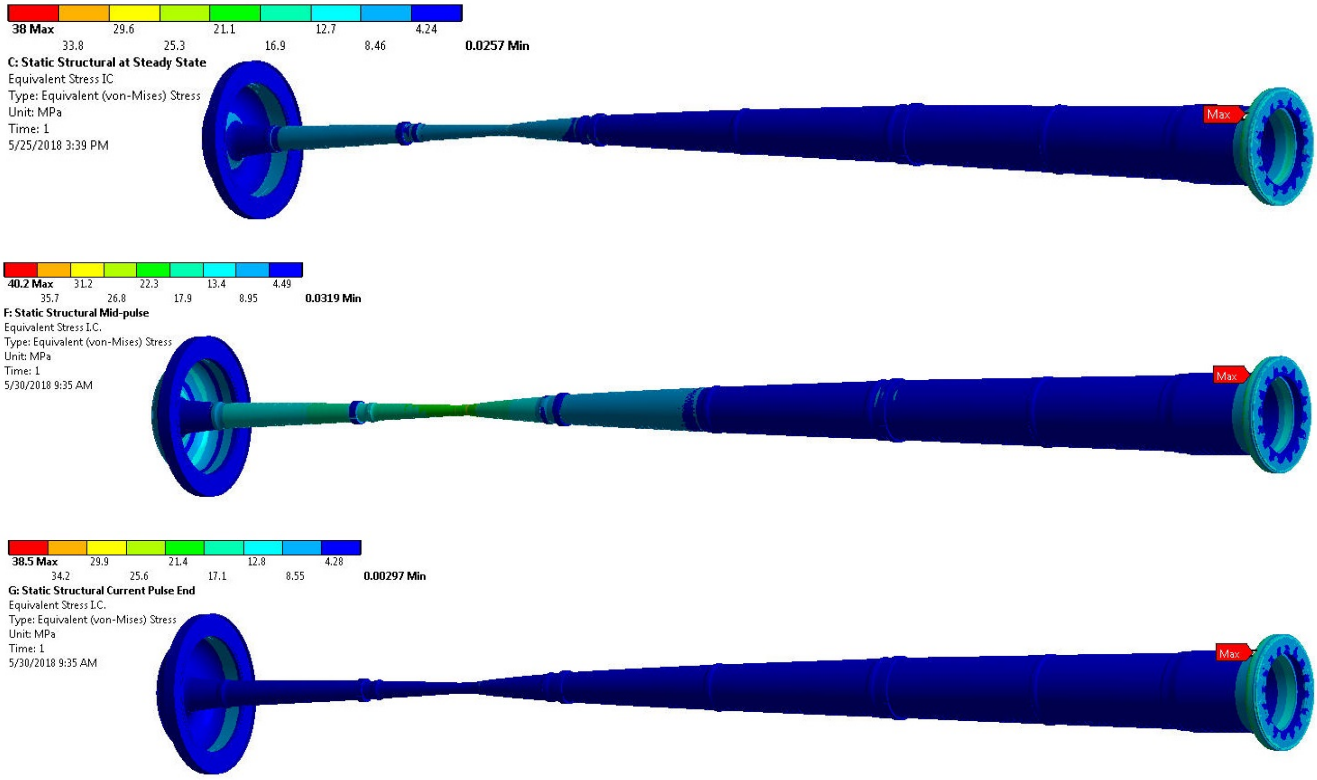

Figure 5.3: Horn1 IC stresses at steady state, mid-pulse and end-pulse

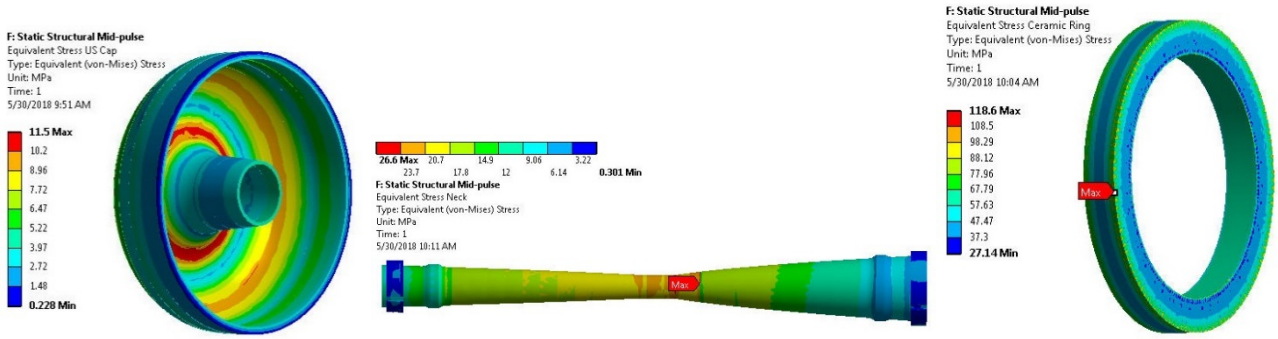

Figure 5.4: Stresses on US cap, Neck and DS ceramic ring at Mid-pulse

During current/beam pulsing, the Neck will get hot while other sections remain relatively cold. The thermal gradients will produce compressive stresses on the neck, meanwhile electromagnetic forces

generate compressive radial stresses on the Neck and tensile axial stresses on the other sections of I.C.. The sections that experience more stress fluctuations as a result of the combination of thermal and magnetic loadings are the Neck and the US cap, shown in Fig. 5.5 and 5.6, respectively.

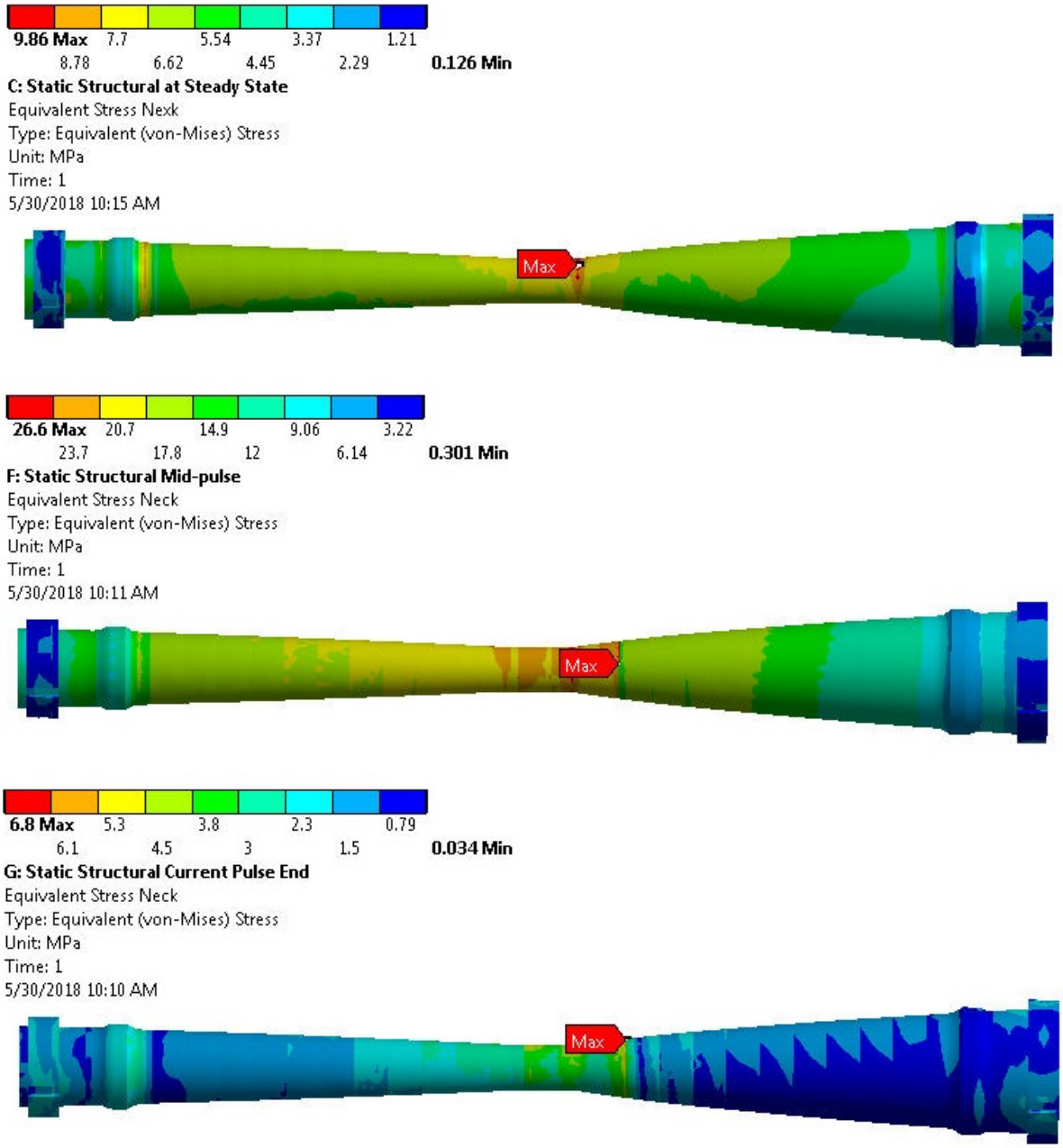

Figure 5.5: Horn-1 Neck stresses at steady state, mid-pulse and end-pulse

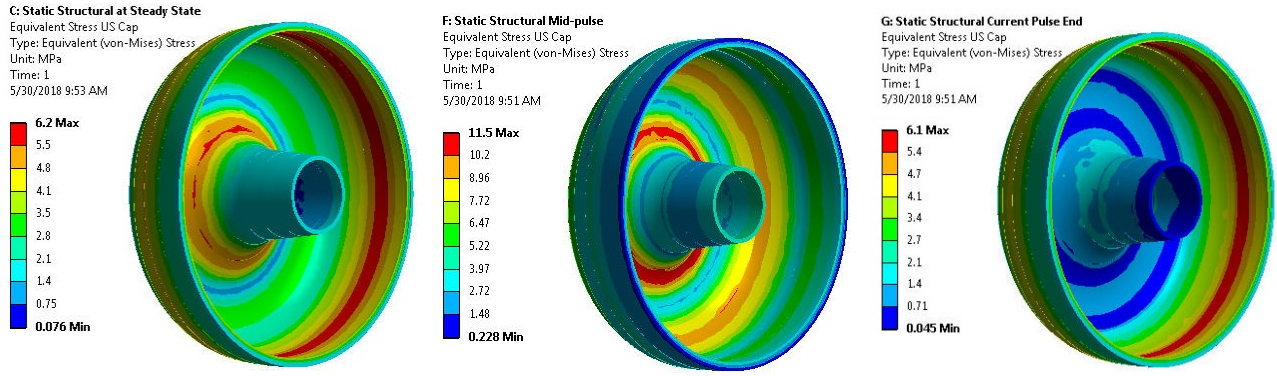

Figure 5.6: US cap stresses at steady state, mid-pulse and end-pulse

The horn displacement in axial and vertical directions at Mid-pulse are shown in Fig. 5.6.

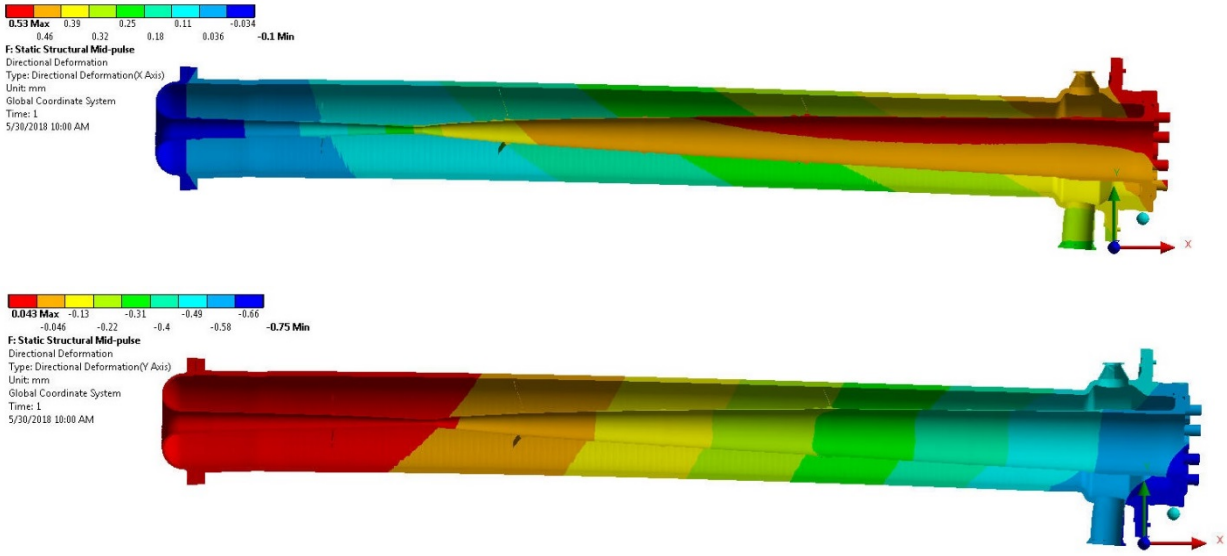

Figure 5.6: Horn displacement in axial and vertical directions at Mid-pulse

6. Fatigue Analysis

From Fig. 5.5 and 5.6, we identified the neck and US transition as the locations experiencing the most stress fluctuations. We further identified the Mid-pulse as the "Max" case and End-pulse as the "Min" case, shown in Fig. 6.1 and 6.2, for fatigue evaluation.

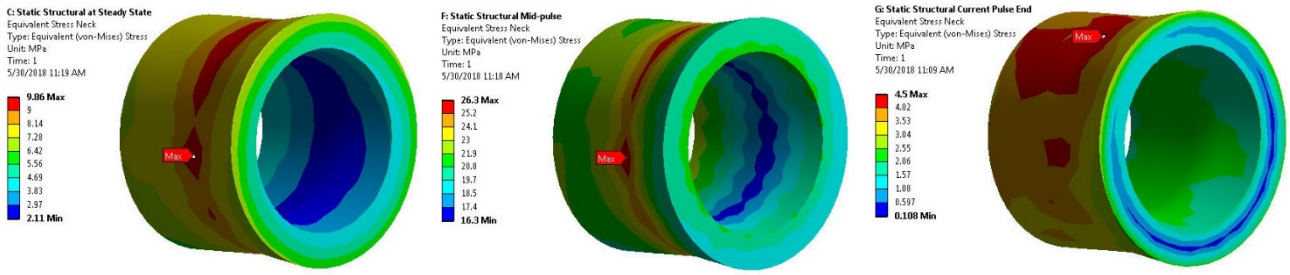

Figure 6.1: Equivalent stresses on a Neck section at steady state, mid-pulse and end-pulse

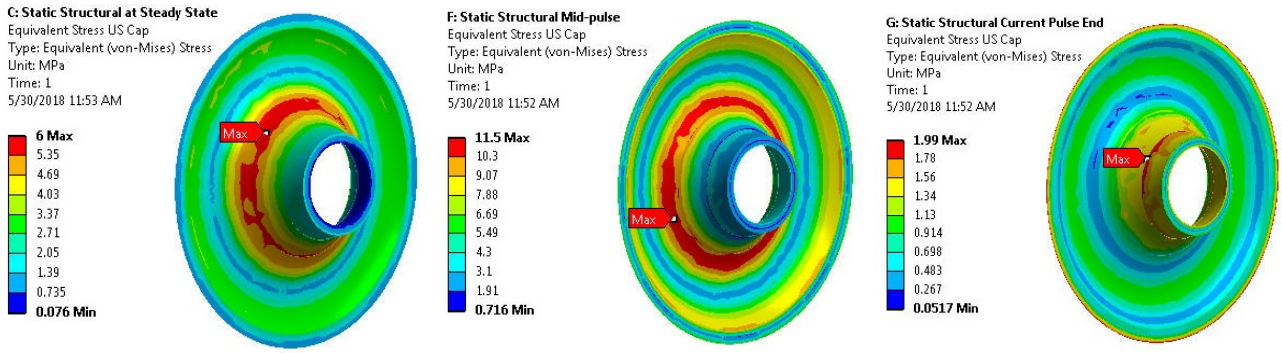

Figure 6.2: Equivalent stresses on US transition at steady state, mid-pulse and end-pulse

Two methods were used to obtain equivalent mean and alternating stresses for fatigue evaluation:
1). Use von-mises equivalent stresses from the FEA results;
2). Use the tri-axial stress tensors from the FEA results, then calculate the equivalent mean and equivalent alternating stresses.

On the modified Goodman fatigue diagram, shown in Fig. 6.3, it gives the endurance limit S_e = 12 KSI (82.7 MPa) and the tensile strength S_{ut} = 44 KSI (303 MPa) for 10^7 cycles constant-life line of aluminum 6061-T6. Using the modified Goodman relation, [10] the fatigue safety factor n can be obtained with:

$$\frac{\sigma_a}{S_e} + \frac{\sigma_m}{S_{ut}} = \frac{1}{n}$$

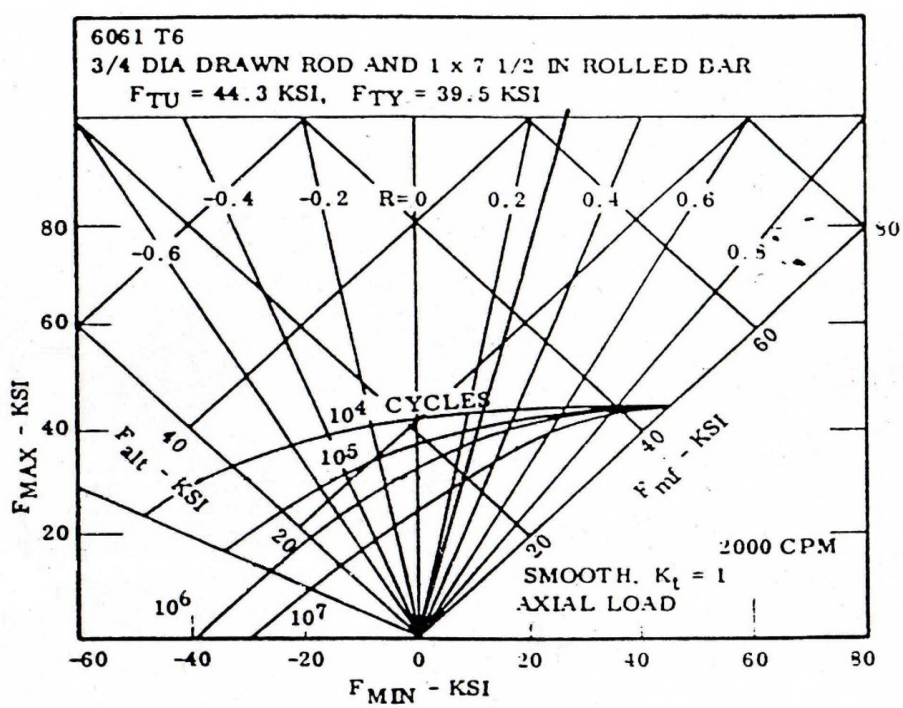

Figure 6.3: Fatigue diagram of Al 6061-T6

6.1 Evaluation with Von-mises Equivalent Stresses – Methord A

For the Neck section, the FEA model contains 1874 nodes. The equivalent stress results from Max and Min cases are plotted in Fig. 6.4.

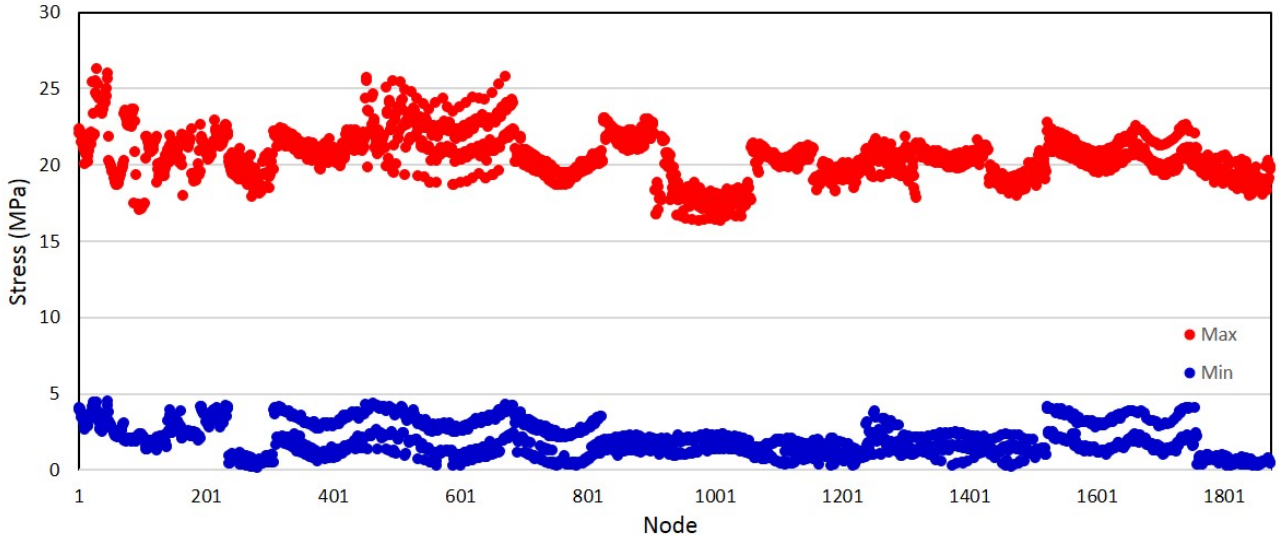

Figure 6.4: Equivalent stresses over Neck's 1874 nodes for the Max and Min cases

Using these values, we obtained the mean stress, alternating stress, stress ratio and the fatigue safety factor for each node. The safety factor is shown in Fig. 6.5. The maximum, minimum and average values are listed in Table 6.1.

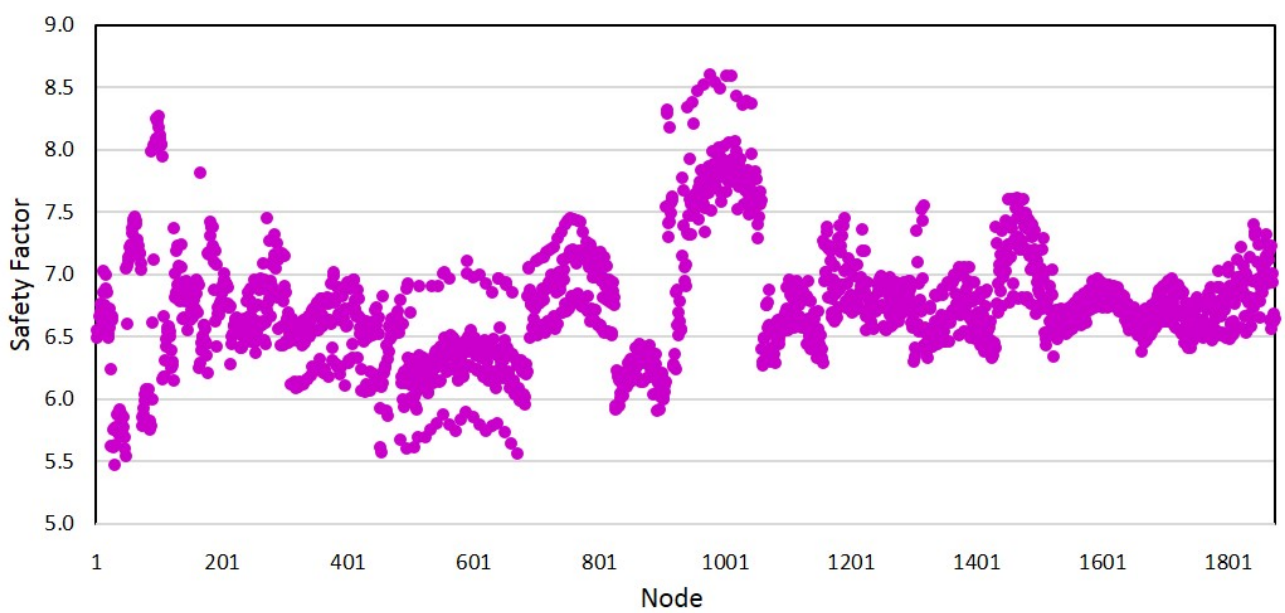

Figure 6.5: Safety factors over Neck's 1874 nodes, using equivalent stresses

Table 6.1: Fatigue evaluation of Neck with equivalent stresses data

		Max	Min	Ave

Mean stress σ_m, MPa	$\sigma_m = \frac{\sigma_{max} + \sigma_{min}}{2}$	15.39 (2.23 KSI)	9.15	11.18
Alternating stress σ_a, MPa	$\sigma_a = \frac{\sigma_{max} - \sigma_{min}}{2}$	10.92 (1.58 KSI)	7.09	9.27
Stress ratio R	$R = \frac{\sigma_{min}}{\sigma_{max}}$	0.2	0.01	0.09
Fatigue safety factor for 10^7 cycles, n	$\frac{\sigma_a}{S_e} + \frac{\sigma_m}{S_{ut}} = \frac{1}{n}$	8.6	5.47	6.74

For the US Cap transition, the FEA model contains 10688 nodes. The stress results from max and Min cases are plotted in Fig. 6.6, the safety factor is shown in Fig. 6.7. The maximum, minimum and average values are listed in Table 6.2.

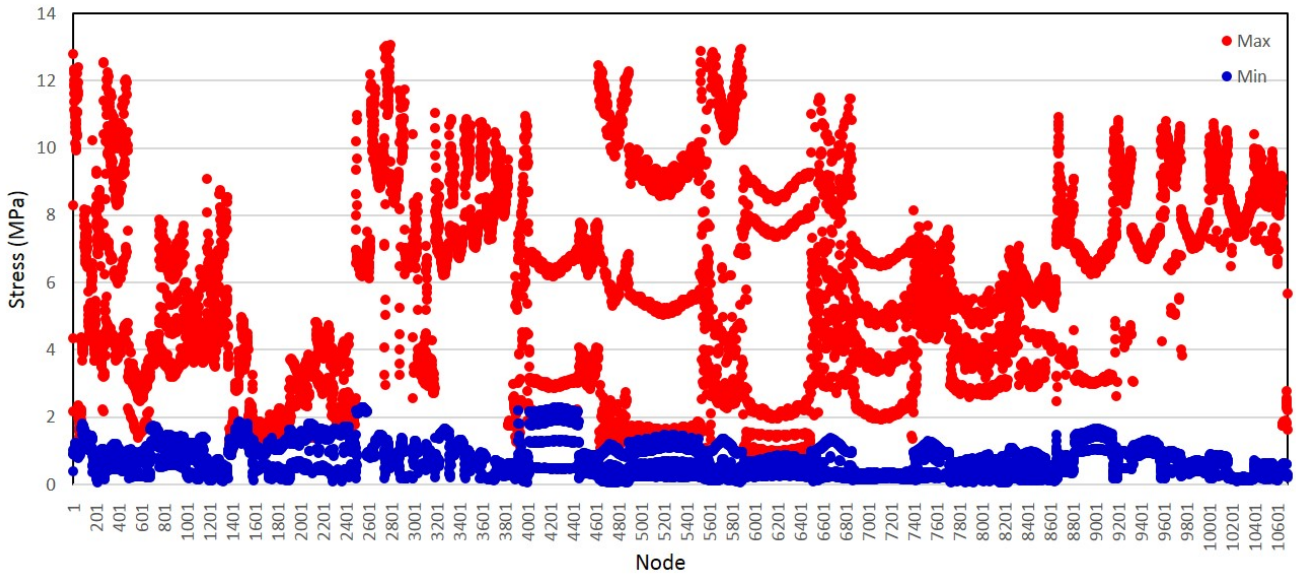

Figure 6.6: Equivalent stresses over US Transition's 10688 nodes for the max and Min cases

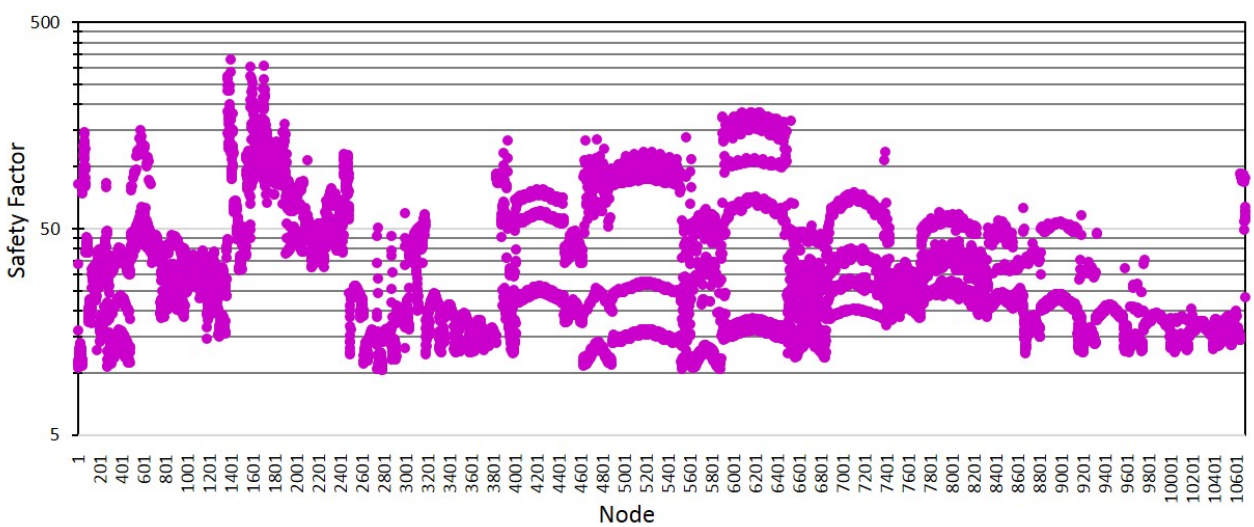

Figure 6.7: Safety factors over US Transition's 10688 nodes, using equivalent stresses

Table 6.2: Fatigue evaluation of US Transition with equivalent stress data

		Max	Min	Ave
Mean stress σ_m, MPa	$\sigma_m = \frac{\sigma_{max} + \sigma_{min}}{2}$	5.90 (0.86 KSI)	0.95	4.18
Alternating stress σ_a, MPa	$\sigma_a = \frac{\sigma_{max} - \sigma_{min}}{2}$	5.01 (0.73 KSI)	0.57	3.45
Stress ratio R	$R = \frac{\sigma_{min}}{\sigma_{max}}$	0.35	0.01	0.11
Fatigue safety factor for 10^7 cycles, n	$\frac{\sigma_a}{S_e} + \frac{\sigma_m}{S_{ut}} = \frac{1}{n}$	92.94	12.49	20.70

6.2 Evaluation with Stress Tensors – Methord B

The stress tensors (normal and shear stresses), shown in Fig. 6.8, are used to calculate the mean and alternating stress cases. Then these values are used to calculate the von-mises equivalent stress values [6].

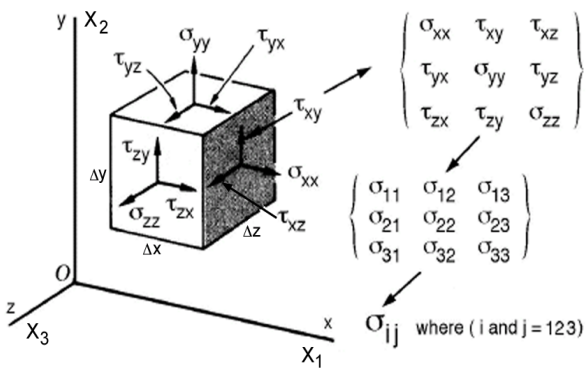

$$\sigma^{eqv} = \sqrt{\frac{(\sigma_1 - \sigma_2)^2 + (\sigma_2 - \sigma_3)^2 + (\sigma_3 - \sigma_1)^2 + 6\left(\sigma_{12}^2 + \sigma_{23}^2 + \sigma_{31}^2\right)}{2}}$$

Figure 6.8: Stress tensors and formula for calculating the von-mises equivalent stress value

The stress tensors for Neck Max and Min cases are shown in Fig. 6.9-10. These values are plotted in Fig. 11-12 for the 1874 nodes. The calculated equivalent stresses and safety factors are plotted in Fig. 13-14.

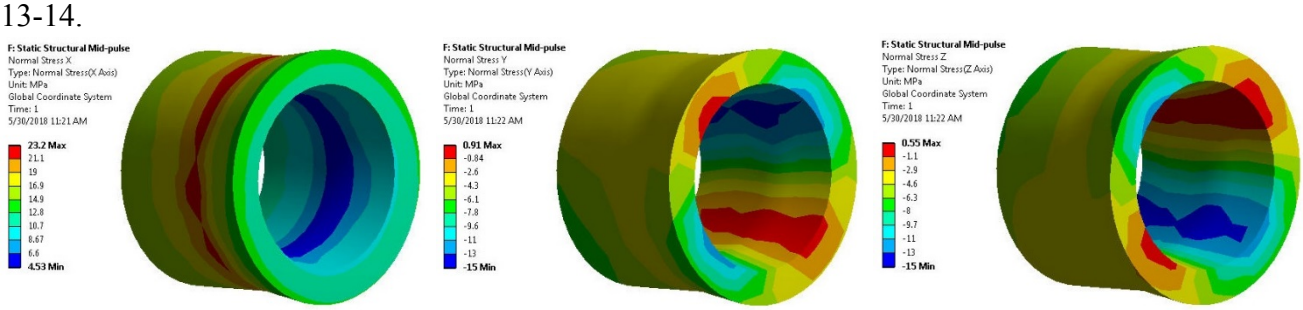

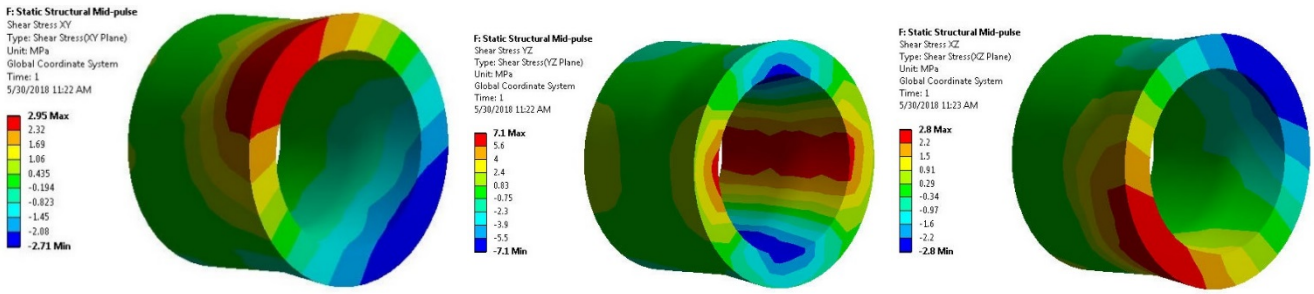

Figure 6.9: Neck stress tensors at Mid-pulse (case Max)

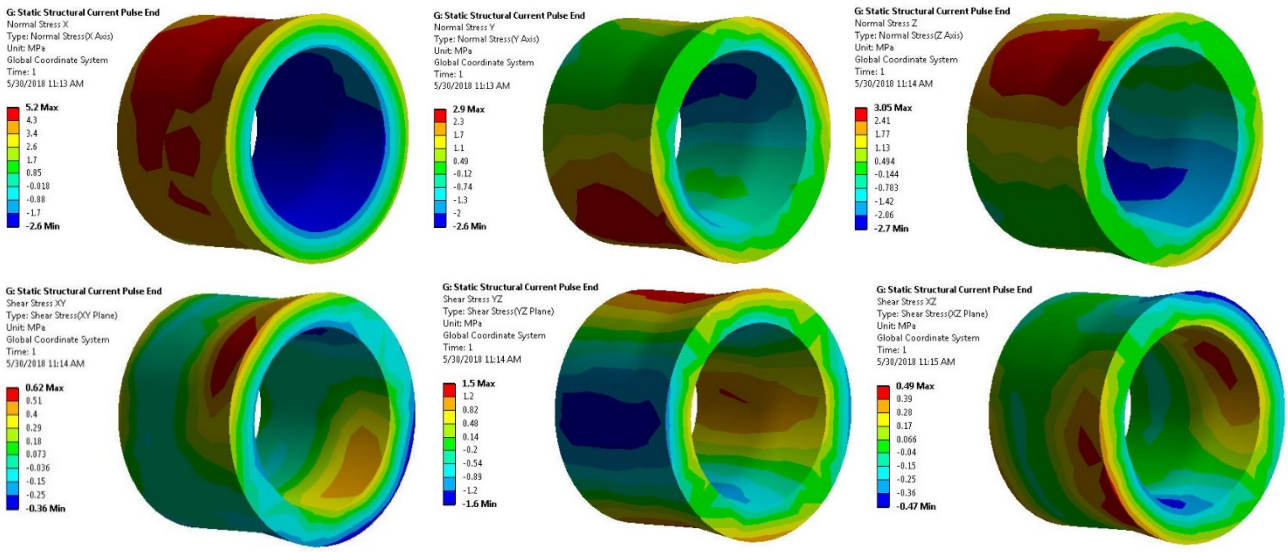

Figure 6.10: Neck stress tensors at End-pulse (case Min)

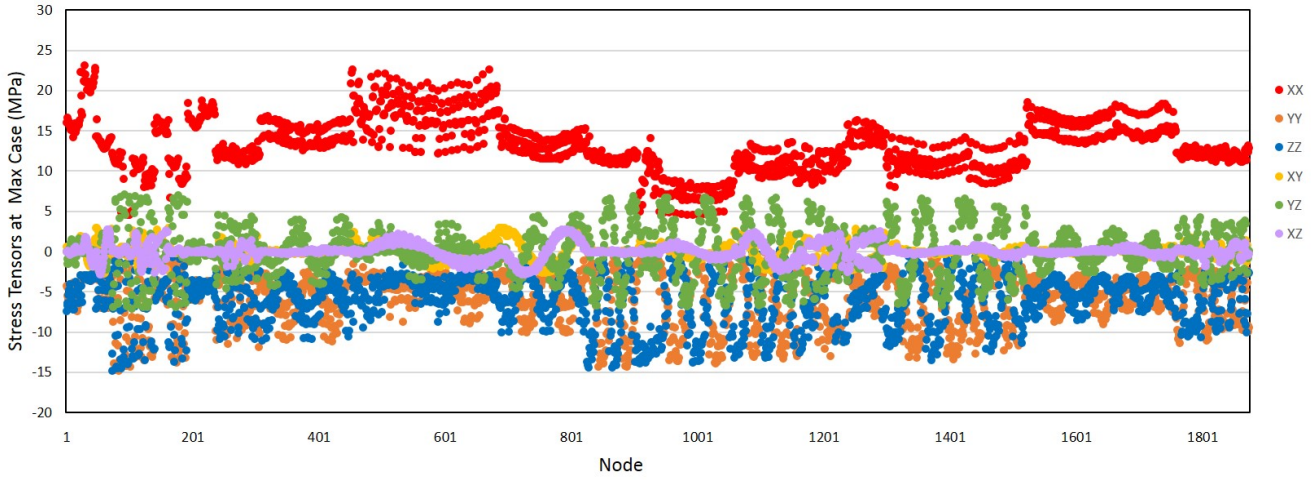

Figure 6.11: Neck stress tensors at Mid-pulse (case Max)

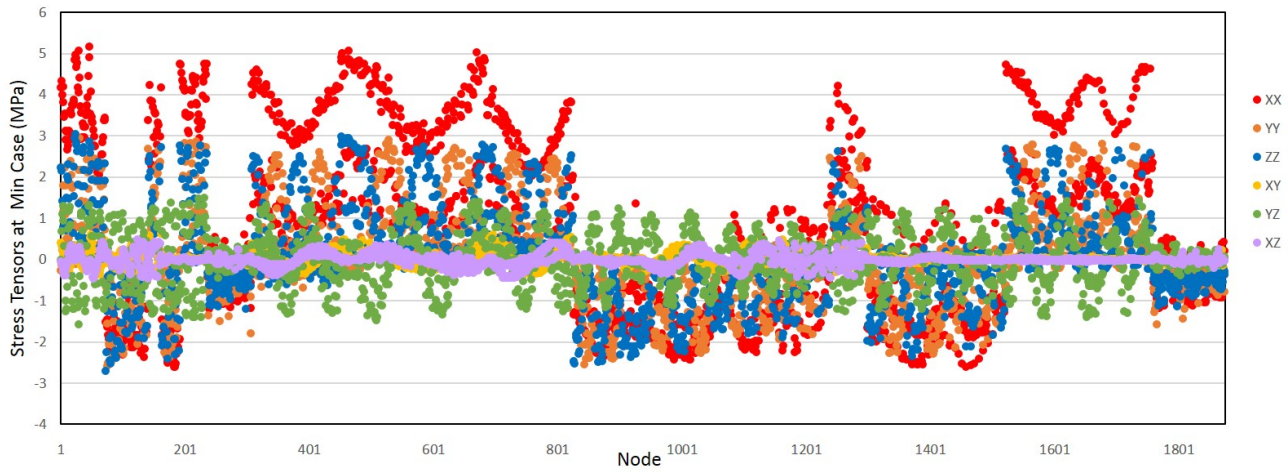

Figure 6.12: Neck stress tensors at End-pulse (case Min)

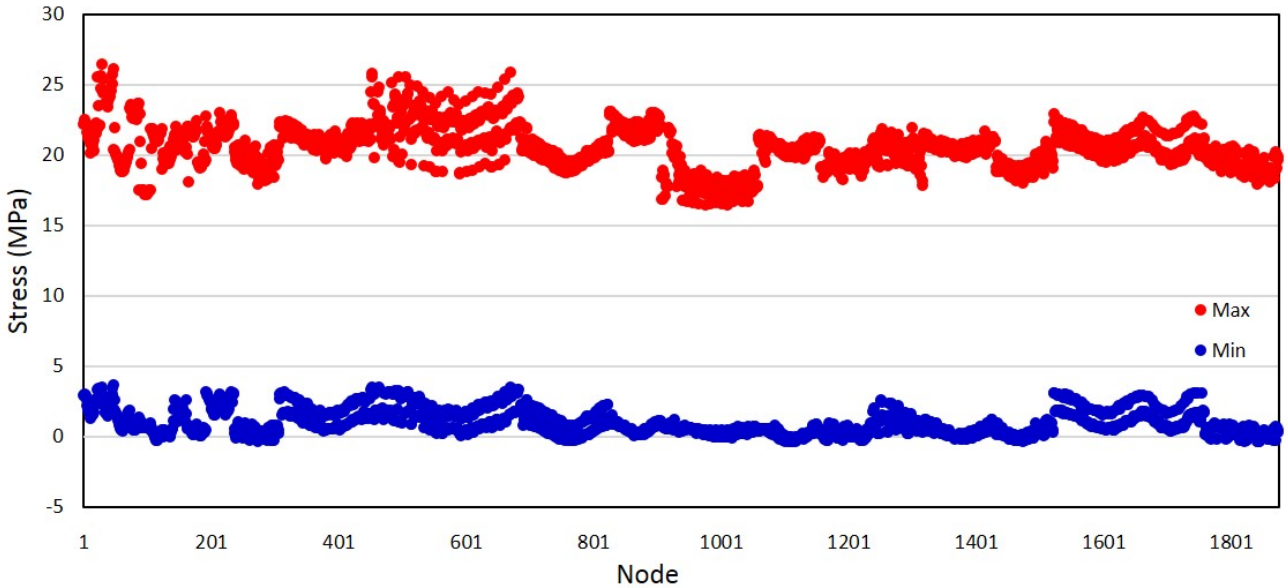

Figure 6.13: Calculated equivalent stresses over Neck's 1874 nodes for the Max and Min cases

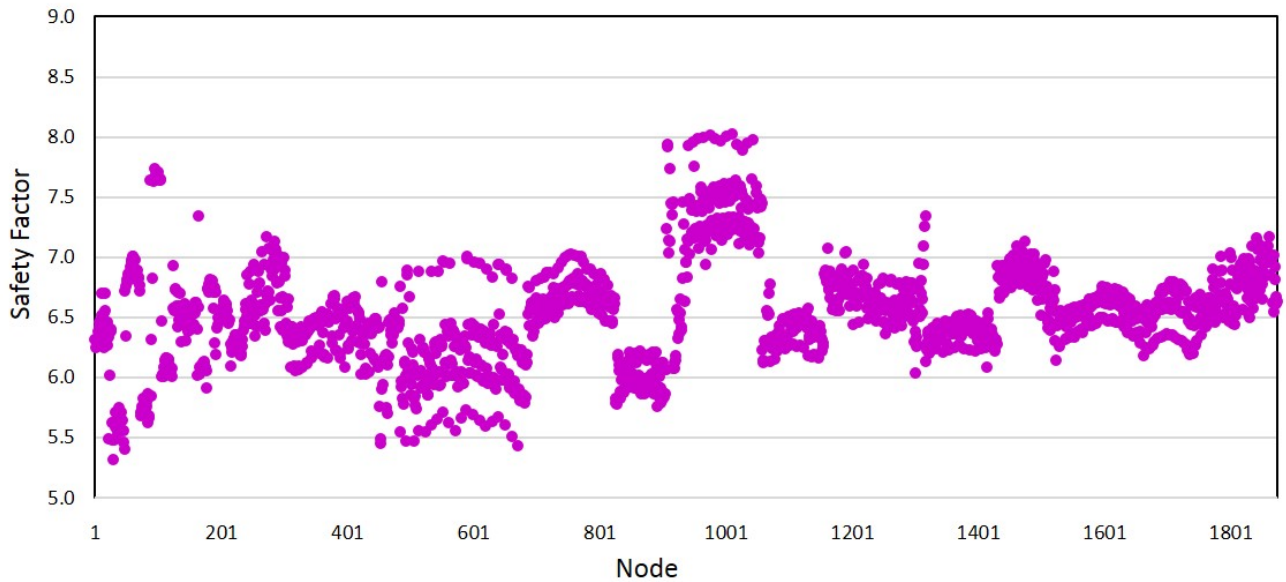

Figure 6.14: Safety factors over Neck's 2066 nodes, using Tri-axial method

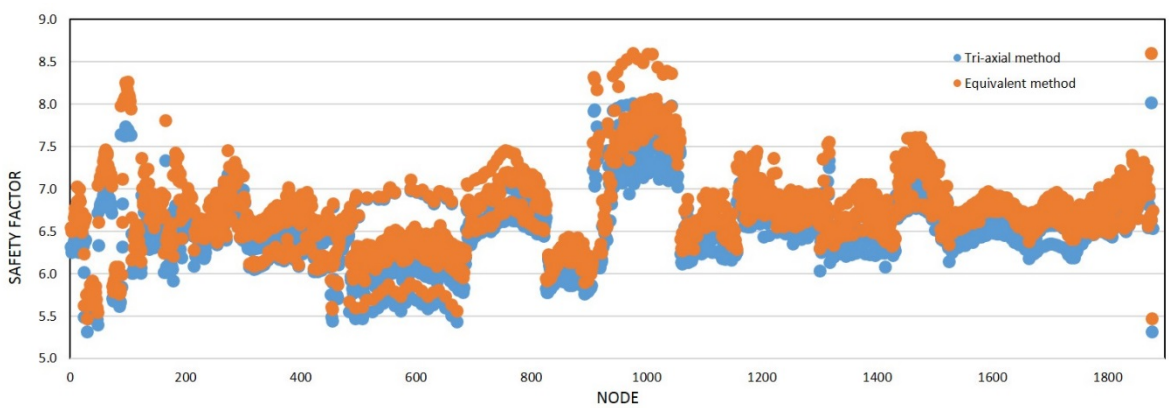

Figure 6.15: Comparison of safety factors with method A and B

The stress tensors for US Cap Max and Min cases are shown in Fig. 6.15-16. The calculated safety factors are plotted in Fig. 17.

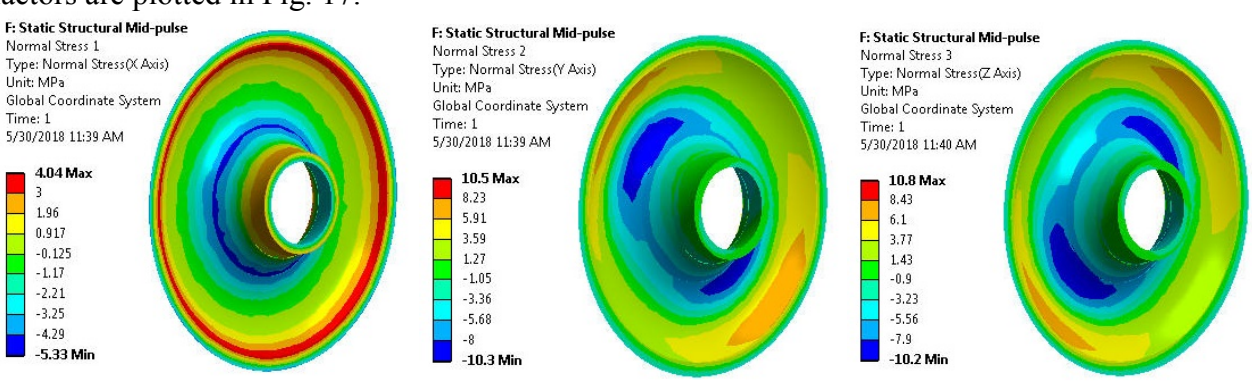

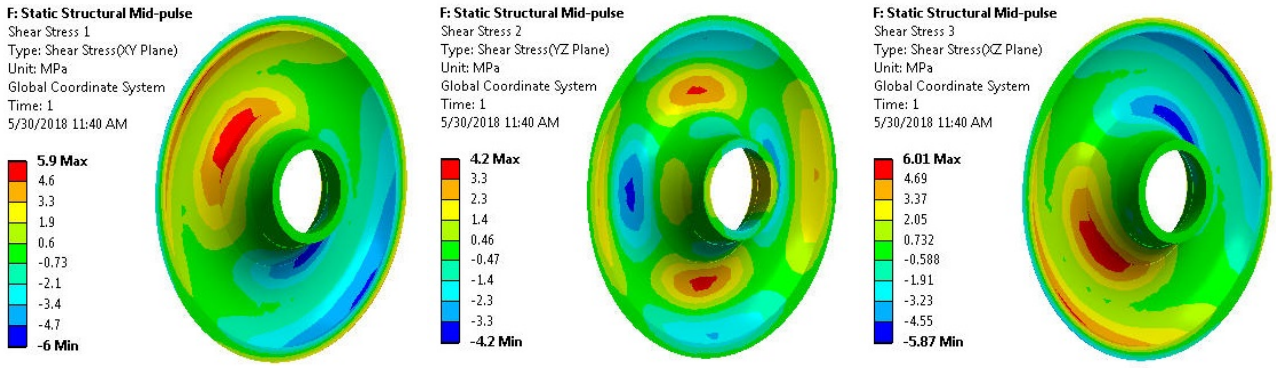

Figure 6.15: US Cap stress tensors at Mid-pulse (case Max)

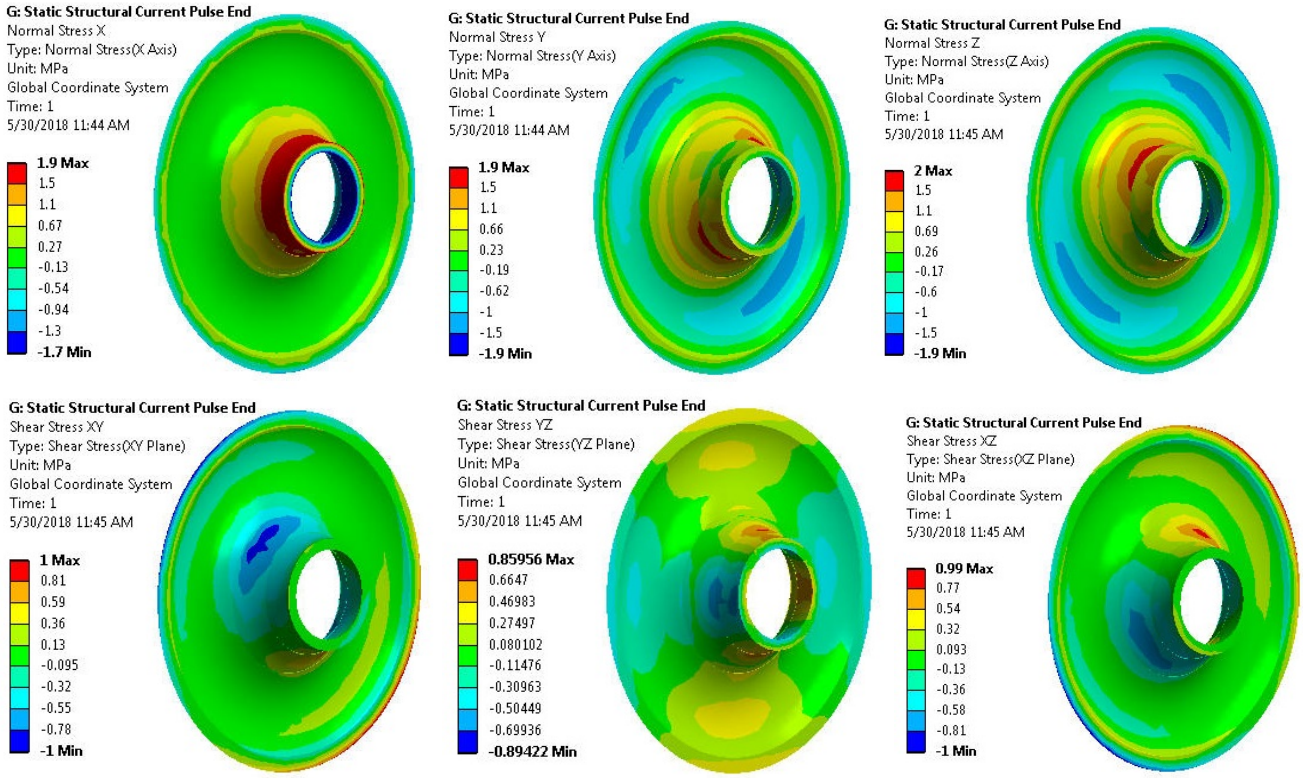

Figure 6.16: US Cap stress tensors at End-pulse (case Min)

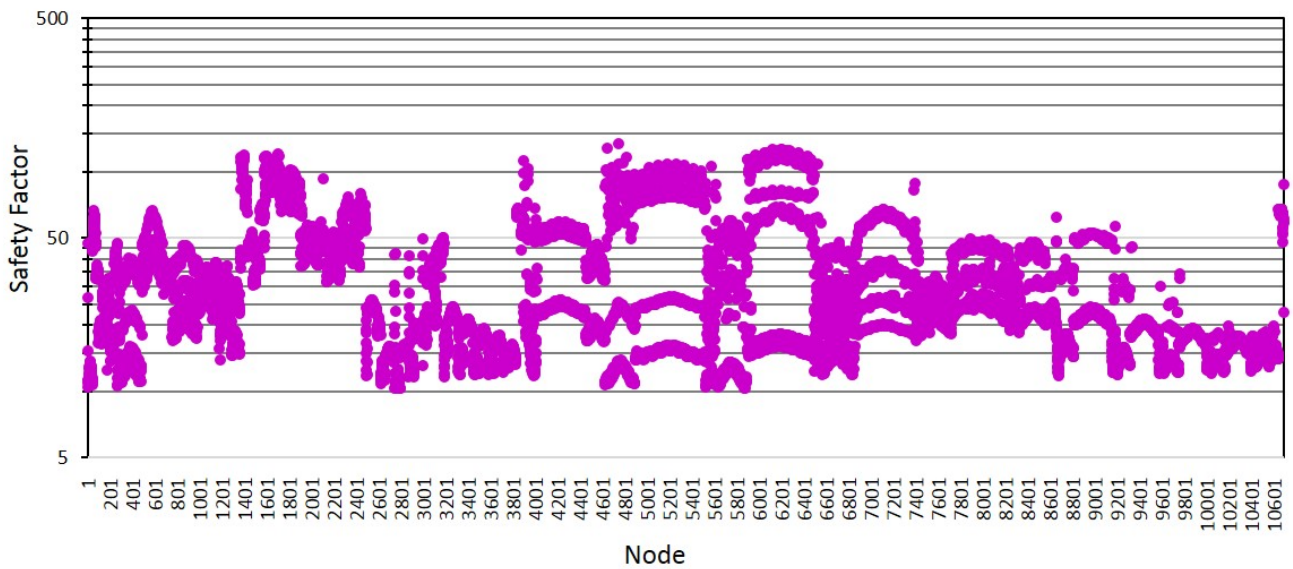

Figure 6.17: Safety factors over US Transition's 10688 nodes, using Tri-axial stresses

6.3 Comparison of two fatigue evaluation methods

A comparison of the results from two methods is summarized in Table 6.3.

Table 6.3: Comparison of Fatigue evaluation of Neck and US transition

		Max	Min	Ave
Neck				
Mean stress σ_m, MPa	Method A	15.39	9.15	11.18
	Method B	15.00	8.45	10.75
Alternating stress σ_a, MPa	Method A	10.92	7.09	9.27
	Method B	11.45	7.99	9.77
Stress ratio R	Method A	0.20	0.01	0.09
	Method B	0.15	-0.02	0.05
Fatigue safety factor for 10^7 cycles, n	Method A	8.60	5.47	6.74
	Method B	8.02	5.32	6.54
US transition				
Mean stress σ_m, MPa	Method A	5.90	0.95	4.18
	Method B	5.47	0.85	4.01
Alternating stress σ_a, MPa	Method A	5.01	0.57	3.45
	Method B	5.48	0.69	3.64
Stress ratio R	Method A	0.35	0.01	0.11
	Method B	0.32	-0.09	0.06
Fatigue safety factor for 10^7 cycles, n	Method A	92.94	12.49	20.70
	Method B	87.34	11.86	19.82

Two methods have a good agreement, though the Tri-axial method is more conservative.

6.4 Fatigue Safety Factor Adjustments

For 10^8 cycles, we have not found a fatigue diagram. Shown in Fig. 6.18, we understand the material fatigue strength for 10^8 cycles is ¾ of the one for 10^7 cycles, if stress ratio is 0.5. For now we scale the safety factor by ¾ of the value for 10^7 cycles,

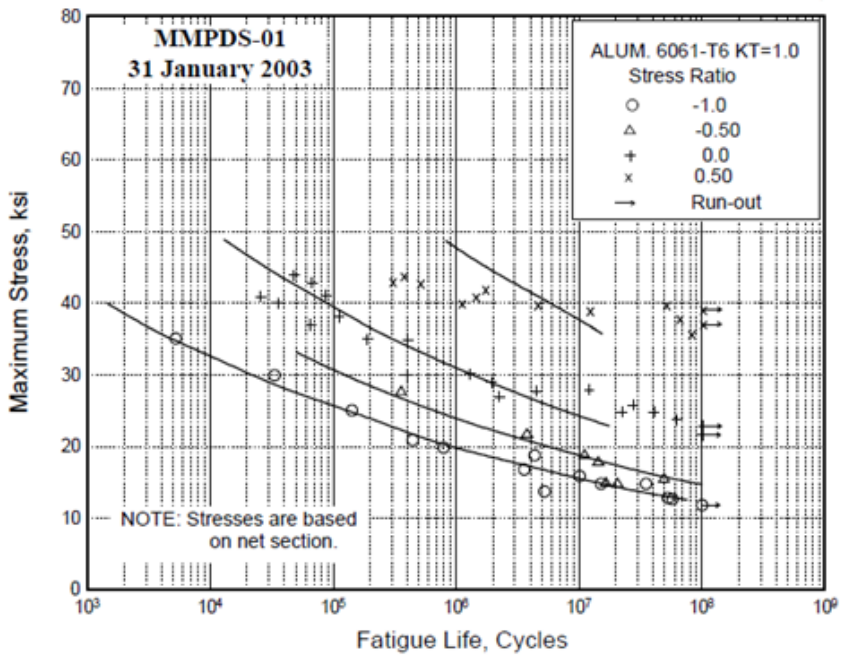

Figure 6.18: Best-fit S/N curves for unnotched 6061-T6 aluminum, longitudinal direction [5]

Table 6.4: Safety factor for 10^8 cycles

	Min
Neck	2
US transition	4.4

7. Other Scenarios

7.1 Thermal Loading Only at Mid-pulse

In order to understand how the thermal load and magnetic load augment or compensate each other, we performed static structural analysis for thermal loading only at mid-pulse and magnetic loading only at a constant room temperature. The results are shown in Fig. 7.1.

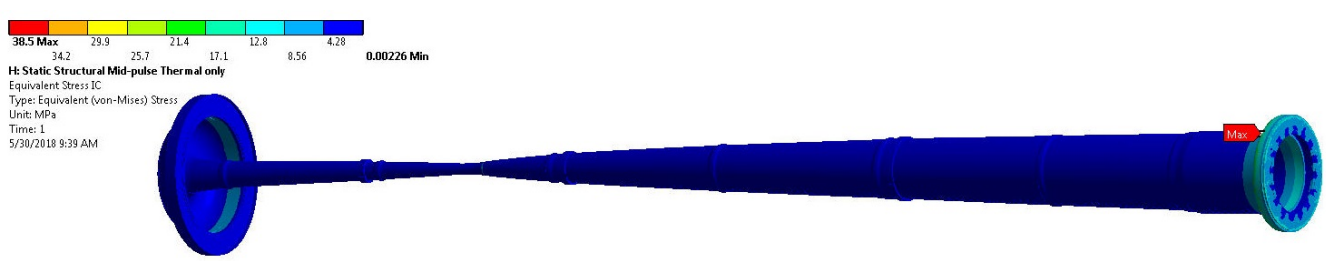

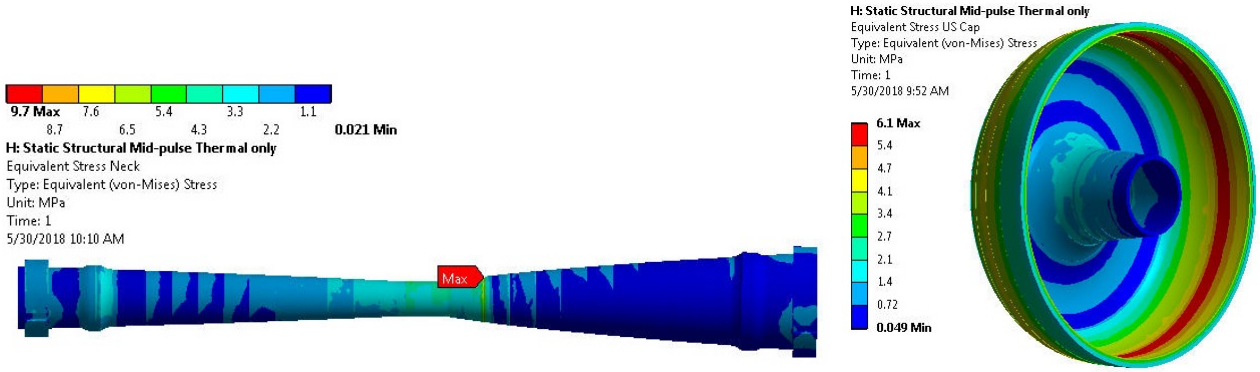

Figure 7.1: Stresses with thermal loading only

7.2 Magnetic Loading Only

In order to understand how the thermal load and magnetic load augment or compensate each other, we performed static structural analysis for thermal loading only at mid-pulse and magnetic loading only at a constant room temperature. The results are shown in Fig. 7.2.

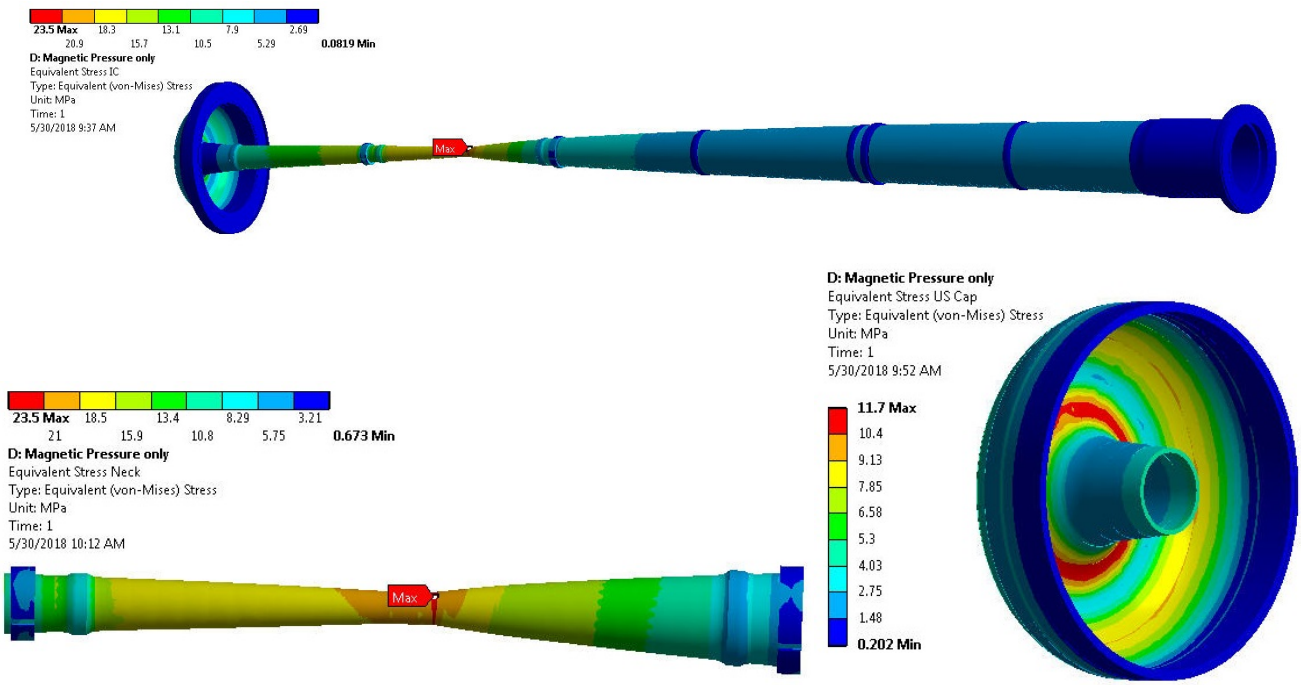

Figure 7.2: Stresses with magnetic pressure loading only

7.3 Current Pulsing Only

There are occasions that Horns are running with current pulses without beam operations. The temperature and stress profiles are shown in Fig. 7.3-7.5.

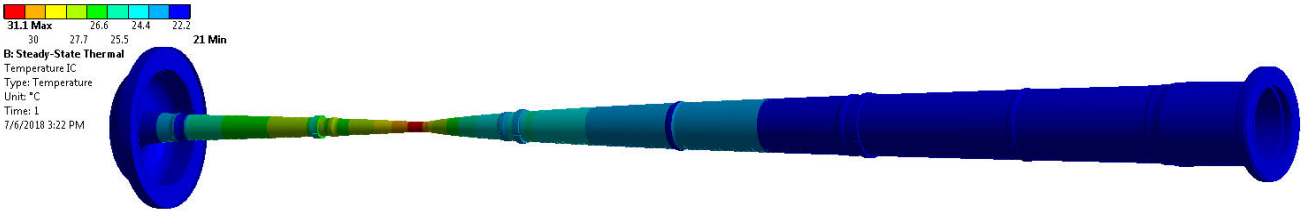

Figure 7.3: Steady state temperature with current pulsing only without beams

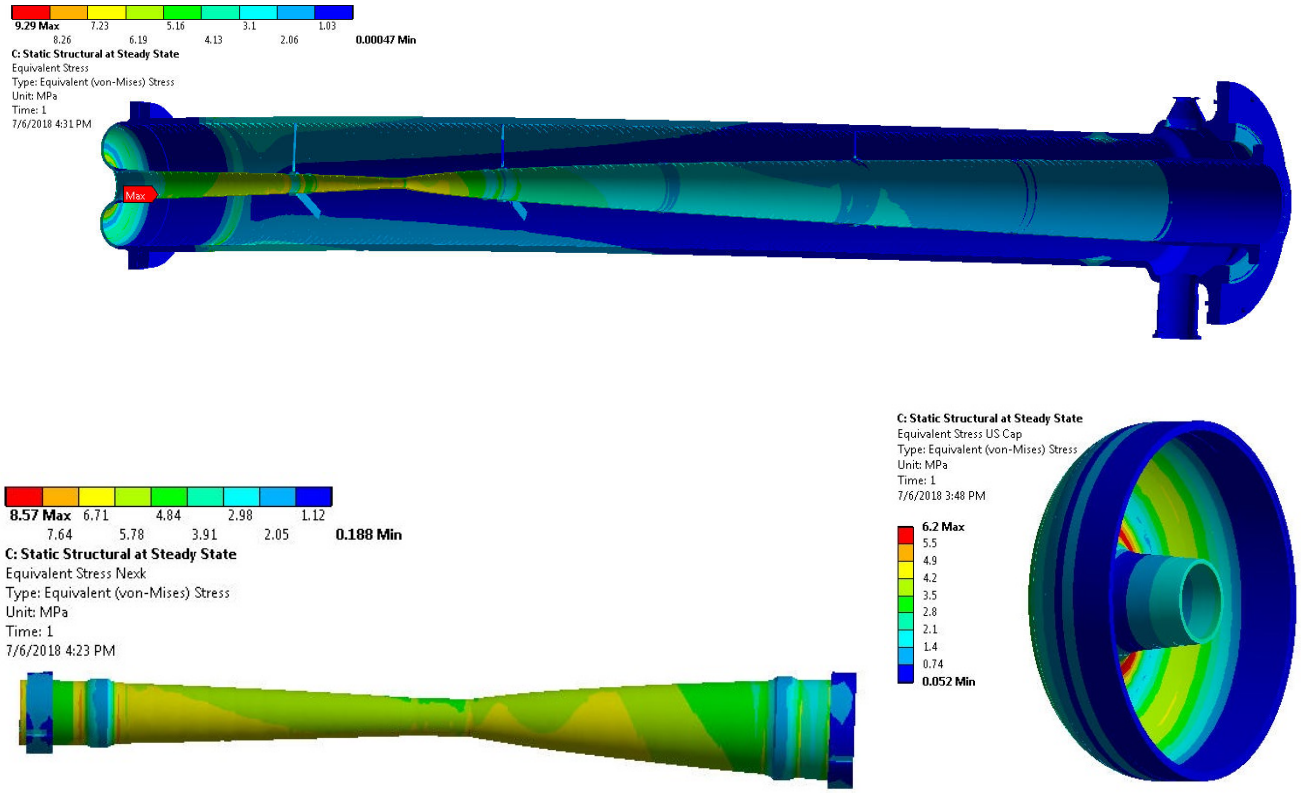

Figure 7.4: Steady state stresses with current pulsing only without beams

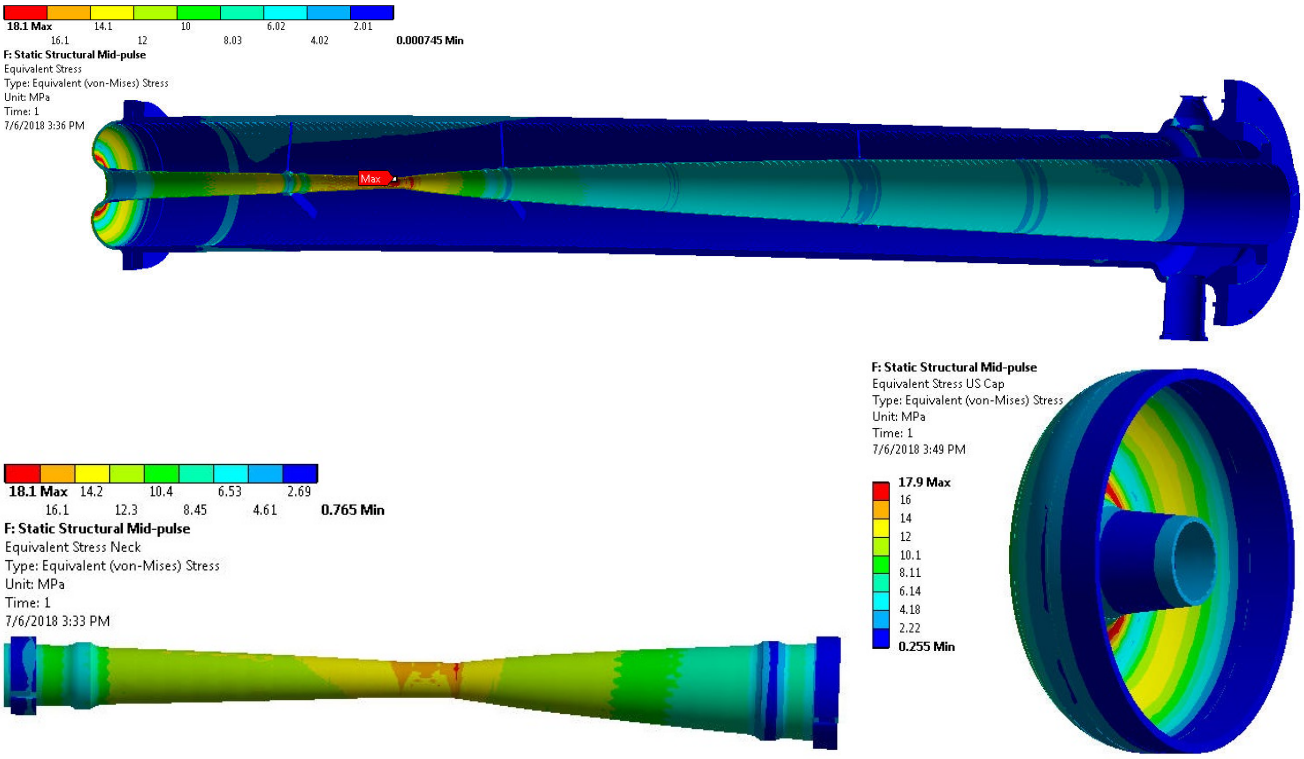

Figure 7.5: Stresses at Mid-pulse with current pulsing only without beams

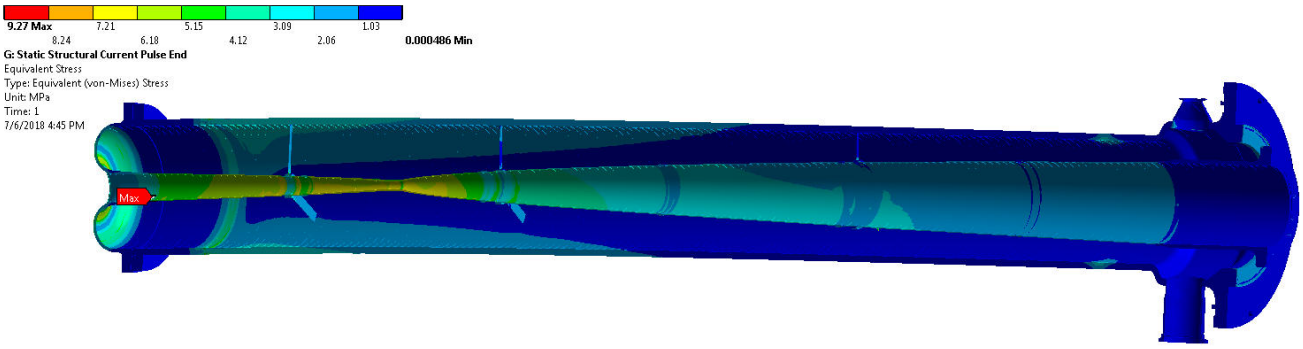

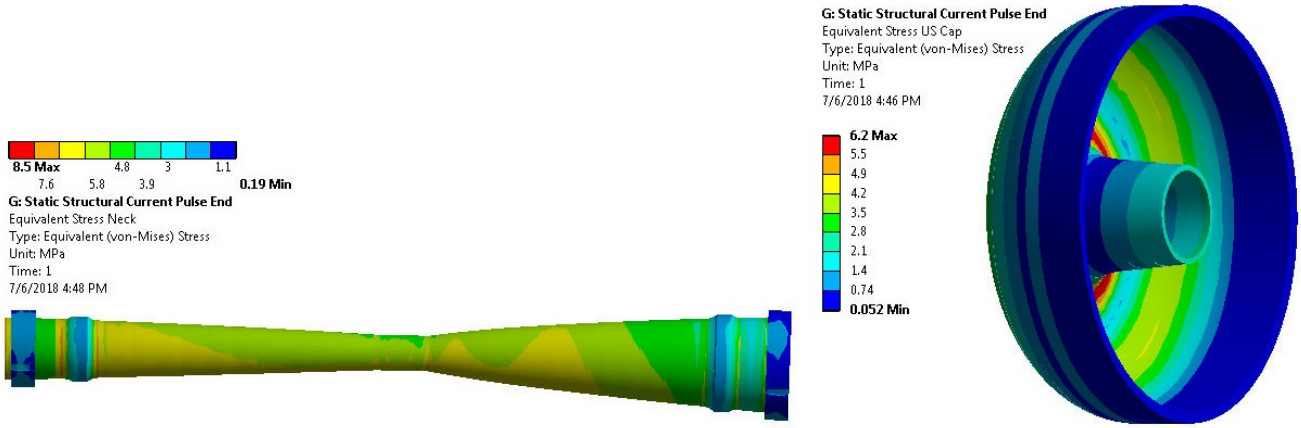

Figure 7.6: Stresses at End-pulse with current pulsing only without beams

7.4 Cold startup

Section 5 and 6 discussed the stresses and fatigue evaluation for the nominal operation after the horn has reached equilibrium status. Here we discuss the stresses at cold startup, shown in Fig. 7.7-7.8.

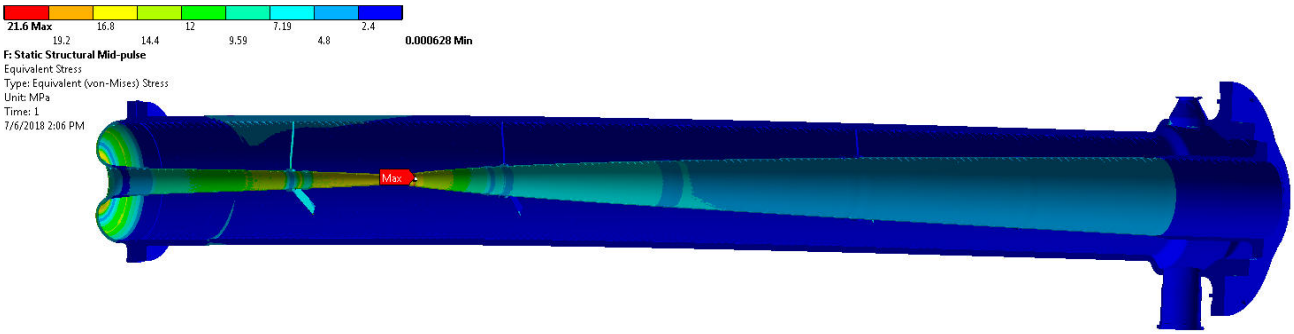

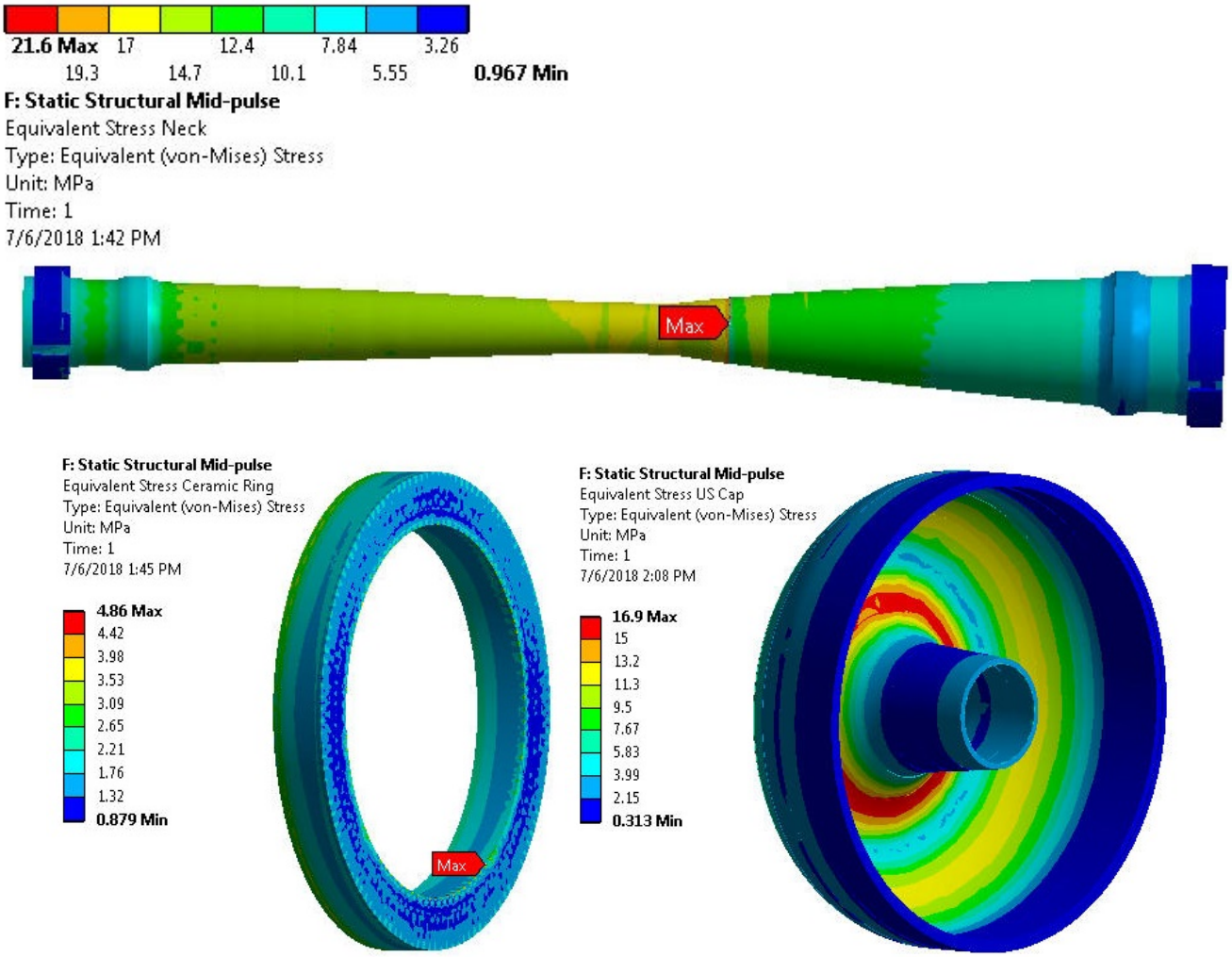

Figure 7.6: Stresses at Beam-end for Cold Startup

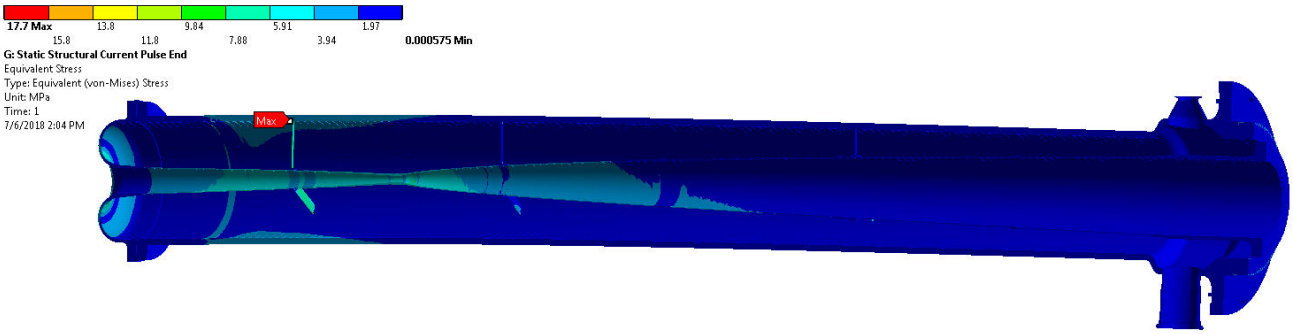

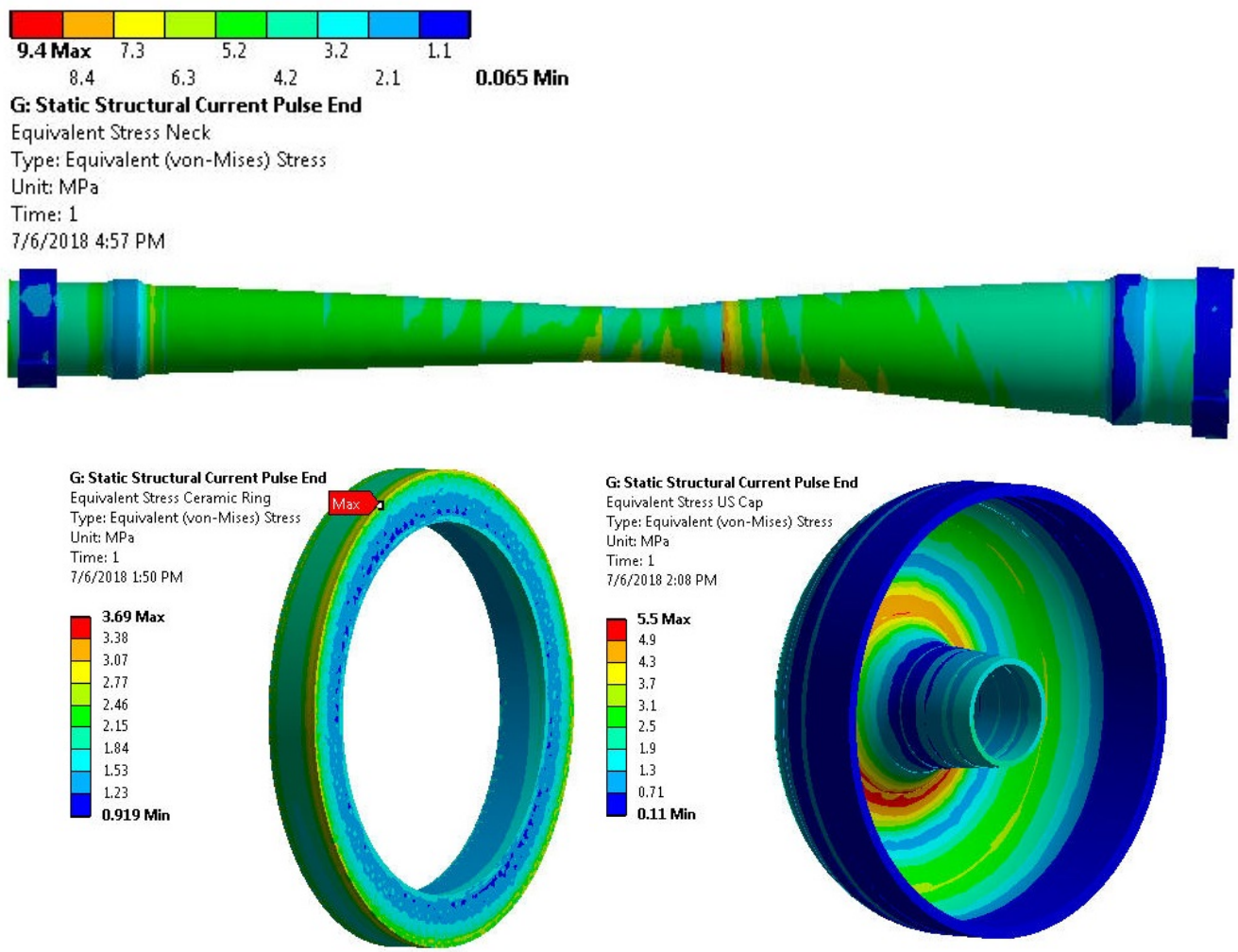

Figure 7.6: Stresses at current-pulse-end for Cold Startup

References

[1] www.matweb.com, Aluminum 6061-T6, Coors Tek Alumina 99.8%
[2] Cory Crowley, LBNE Horn 1 inner conductor cooling test study, Feb. 19, 2013
[3] Cory Crowley, NuMI Horn1 inner conductor cooling coefficient estimate, May 15, 2018
[4] Online calculator
[5] Igor Rakhno, Horn 1 MARS energy deposition analysis for 1 MW
[6] Patrick Hurh, Tri-axial fatigue evaluation spreadsheet, Oct. 19, 2017

Appendix I: Thermal Loads of Horn 1 at Steady State

Table I-a: Geometrical dimensions and heating loads of Horn1 inner conductor at steady state

Bin No.	Z	Volume	Thickness	Mid-radius	Resistive Heating		Beam Heating			Total heating
	cm	cm³	cm	cm	W/cm³	W	GeV/cm³-proton)	W/cm³	W	W/cm³
9	US Flange	1490	14.45	13.4	0.0	0.2	3.99E-05	0.3	515.3	0.3

8	CAP	220	0.81	5.8	0.2	38.2	5.76E-05	0.5	109.8	0.7
7	CAP	158	0.81	5.8	0.2	27.6	6.02E-05	0.5	82.7	0.7
6	CAP	160	0.81	5.8	0.2	27.8	6.13E-05	0.5	84.9	0.7
5	CAP	180	0.81	5.8	0.2	31.3	7.74E-05	0.7	120.7	0.8
1	0	418	0.81	5.8	0.2	72.7	1.24E-04	1.1	448.3	1.2
2	2	62	0.81	5.8	0.2	10.7	2.39E-04	2.1	128.1	2.3
3	4	42	0.81	5.8	0.2	7.2	3.80E-04	3.3	137.0	3.5
4	6	35	0.81	5.8	0.2	6.1	4.89E-04	4.2	147.3	4.4
11	8	27	0.81	8.4	0.1	2.3	5.71E-04	5.0	135.9	5.0
12	10	21	0.64	3.7	0.7	13.9	6.35E-04	5.5	113.3	6.2
13	12	15	0.47	3.6	1.4	20.5	6.94E-04	6.0	89.7	7.4
14	14	18	0.30	3.6	3.4	62.5	7.49E-04	6.5	117.9	9.9
1	16	8	0.20	3.2	9.8	80.0	7.42E-04	6.4	52.6	16.2
2	18	8	0.20	3.1	10.1	81.8	7.35E-04	6.4	51.4	16.5
3	20	8	0.20	3.1	10.5	83.8	7.21E-04	6.3	49.9	16.8
4	22	8	0.20	3.0	10.9	85.5	7.25E-04	6.3	49.5	17.2
5	24	8	0.20	3.0	11.2	87.2	7.23E-04	6.3	48.7	17.5
6	26	8	0.20	2.9	11.6	88.6	7.36E-04	6.4	48.8	18.0
7	28	8	0.20	2.9	12.1	90.8	7.38E-04	6.4	48.2	18.5
8	30	7	0.20	2.8	12.5	92.7	7.55E-04	6.6	48.5	19.1
9	32	7	0.20	2.8	13.1	95.0	7.67E-04	6.7	48.4	19.7
10	34	7	0.20	2.7	13.6	96.9	7.72E-04	6.7	47.9	20.3
11	36	7	0.20	2.7	14.2	99.2	7.99E-04	6.9	48.6	21.1
12	38	7	0.20	2.6	14.7	100.8	8.01E-04	7.0	47.8	21.6
13	40	7	0.20	2.6	15.3	102.9	8.17E-04	7.1	47.7	22.4
14	42	7	0.20	2.5	15.9	104.5	1.02E-03	8.8	58.1	24.7
15	44	6	0.20	2.5	16.5	106.2	1.10E-03	9.5	61.1	26.0
16	46	6	0.20	2.4	16.9	106.4	9.37E-04	8.1	51.2	25.1
17	48	6	0.20	2.4	17.9	112.0	9.16E-04	8.0	49.8	25.8
18	50	6	0.21	2.4	16.7	104.7	9.31E-04	8.1	50.8	24.7
19	52	6	0.21	2.3	16.5	104.5	9.46E-04	8.2	51.9	24.7
20	54	20	0.81	2.6	0.9	18.6	9.61E-04	8.3	169.9	9.3
21	56	11	0.22	2.2	16.4	176.9	1.01E-03	8.7	94.1	25.1
22	58	10	0.48	2.2	3.4	32.5	1.02E-03	8.9	85.7	12.2
23	60	9	0.24	2.1	16.5	153.9	1.08E-03	9.3	86.8	25.9
24	62	6	0.25	2.0	16.6	102.5	1.10E-03	9.6	59.2	26.2
25	64	6	0.26	1.9	16.7	102.8	1.16E-03	10.1	62.1	26.7
26	66	6	0.27	1.8	16.7	103.7	1.20E-03	10.4	64.6	27.1
27	68	6	0.28	1.8	16.8	105.1	1.24E-03	10.8	67.3	27.5
28	70	6	0.29	1.7	16.8	106.7	1.33E-03	11.5	72.8	28.3
29	72	6	0.31	1.6	16.9	108.4	1.37E-03	11.9	76.3	28.8

30	74	6	0.33	1.5	17.0	110.0	1.43E-03	12.4	80.4	29.4
31	76	7	0.35	1.4	17.0	111.1	1.51E-03	13.1	85.6	30.1
32	78	7	0.38	1.3	17.1	111.7	1.63E-03	14.2	92.7	31.3
33	80	6	0.42	1.2	17.1	111.3	1.72E-03	14.9	97.0	32.1
34	82	6	0.44	1.1	16.6	105.9	1.74E-03	15.1	96.5	31.7
35	84	6	0.45	1.1	16.1	102.4	2.10E-03	18.2	115.8	34.3
36	86	6	0.45	1.1	16.0	101.5	2.26E-03	19.6	124.6	35.6
37	88	6	0.37	1.3	16.9	105.3	2.32E-03	20.1	125.2	37.0
38	90	6	0.30	1.6	16.8	108.0	1.26E-03	10.9	70.4	27.7
39	92	7	0.26	1.9	16.7	110.0	9.94E-04	8.6	57.0	25.3
40	94	6	0.23	2.1	16.5	105.0	8.34E-04	7.2	45.9	23.8
41	96	6	0.21	2.3	16.4	100.4	7.54E-04	6.5	40.0	23.0
42	98	6	0.20	2.5	15.5	98.7	7.03E-04	6.1	38.7	21.6
43	100	7	0.20	2.7	13.6	93.5	6.49E-04	5.6	38.7	19.2
44	102	7	0.20	2.8	11.9	87.0	6.16E-04	5.3	39.2	17.2
45	104	8	0.20	3.0	11.0	84.9	5.82E-04	5.1	39.2	16.0
46	106	8	0.20	3.1	10.3	83.1	5.52E-04	4.8	38.7	15.1
47	108	10	0.20	3.3	9.4	90.3	5.28E-04	4.6	44.2	13.9
48	110	19	0.47	3.5	1.4	26.1	5.06E-04	4.4	82.0	5.8
49	112	9	0.20	3.5	7.8	72.4	4.77E-04	4.1	38.3	12.0
50	114	33	0.70	3.9	0.5	17.0	4.78E-04	4.1	135.5	4.7
51	116	11	0.20	3.8	6.9	73.1	5.28E-04	4.6	48.4	11.5
52	118	10	0.20	3.9	6.4	66.0	4.73E-04	4.1	42.0	10.5
53	120	10	0.20	4.3	5.3	55.8	4.46E-04	3.9	40.5	9.2
54	122	11	0.20	4.4	5.1	54.4	4.28E-04	3.7	39.7	8.8
55	124	11	0.20	4.5	4.9	52.9	4.06E-04	3.5	38.4	8.4
56	126	11	0.20	4.6	4.6	51.3	3.88E-04	3.4	37.4	8.0
57	128	11	0.20	4.7	4.4	50.2	3.67E-04	3.2	36.0	7.6
58	130	11	0.20	4.8	4.3	49.0	3.52E-04	3.1	35.0	7.3
59	132	12	0.20	4.9	4.1	47.9	3.41E-04	3.0	34.5	7.1
60	134	12	0.20	5.0	4.0	46.8	3.33E-04	2.9	34.1	6.8
61	136	12	0.20	5.1	3.8	45.5	3.26E-04	2.8	33.9	6.6
62	138	12	0.20	5.1	3.6	44.3	3.14E-04	2.7	33.1	6.4
63	140	12	0.20	5.2	3.5	43.4	3.10E-04	2.7	33.4	6.2
64	142	13	0.20	5.3	3.4	42.7	3.03E-04	2.6	33.4	6.0
65	144	13	0.20	5.4	3.2	42.2	2.91E-04	2.5	32.9	5.8
66	146	13	0.20	5.5	3.1	41.5	2.83E-04	2.5	32.9	5.6
67	148	14	0.20	5.6	3.0	41.3	2.77E-04	2.4	32.8	5.4
68	150	14	0.20	5.6	2.9	41.0	2.73E-04	2.4	33.0	5.3
69	152	14	0.20	5.7	2.9	40.6	2.65E-04	2.3	32.6	5.2
70	154	14	0.20	5.8	2.8	40.2	2.58E-04	2.2	32.2	5.0

71	156	15	0.20	5.9	2.7	39.7	2.52E-04	2.2	31.9	4.9
72	158	15	0.20	5.9	2.7	39.4	2.49E-04	2.2	32.0	4.8
73	160	32	0.20	6.0	2.6	83.5	2.43E-04	2.1	67.3	4.7
74	162	17	0.20	6.1	2.6	43.9	2.43E-04	2.1	36.1	4.7
75	164	15	0.20	6.2	2.5	38.3	2.35E-04	2.0	31.1	4.6
76	166	15	0.20	6.2	2.5	37.9	2.29E-04	2.0	30.6	4.5
77	168	16	0.20	6.3	2.4	37.4	2.27E-04	2.0	30.5	4.4
78	170	16	0.20	6.4	2.4	37.0	2.20E-04	1.9	29.9	4.3
79	172	16	0.20	6.5	2.3	36.5	2.18E-04	1.9	30.0	4.2
80	174	16	0.20	6.5	2.3	36.1	2.14E-04	1.9	29.6	4.1
81	176	16	0.20	6.6	2.2	35.7	2.12E-04	1.8	29.8	4.1
82	178	16	0.20	6.7	2.2	35.4	2.06E-04	1.8	29.3	4.0
83	180	17	0.20	6.7	2.1	35.1	2.03E-04	1.8	29.1	3.9
84	182	17	0.20	6.8	2.1	34.9	2.02E-04	1.8	29.3	3.8
85	184	17	0.20	6.9	2.0	34.6	1.95E-04	1.7	28.6	3.7
86	186	17	0.20	6.9	2.0	34.2	1.97E-04	1.7	29.2	3.7
87	188	17	0.20	7.0	2.0	34.0	1.92E-04	1.7	28.7	3.6
88	190	17	0.20	7.1	1.9	33.7	1.89E-04	1.6	28.5	3.6
89	192	18	0.20	7.1	1.9	33.4	1.89E-04	1.6	28.8	3.5
90	194	18	0.20	7.2	1.9	33.1	1.83E-04	1.6	28.1	3.5
91	196	18	0.20	7.2	1.8	32.8	1.82E-04	1.6	28.2	3.4
92	198	18	0.20	7.3	1.8	32.5	1.81E-04	1.6	28.3	3.4
93	200	18	0.20	7.4	1.8	32.3	1.77E-04	1.5	27.9	3.3
94	202	18	0.20	7.4	1.7	32.0	1.73E-04	1.5	27.5	3.2
95	204	18	0.20	7.5	1.7	31.7	1.70E-04	1.5	27.3	3.2
96	206	19	0.20	7.6	1.7	31.5	1.69E-04	1.5	27.3	3.2
97	208	19	0.20	7.6	1.7	31.2	1.65E-04	1.4	27.0	3.1
98	210	30	0.20	7.7	1.6	49.0	1.64E-04	1.4	42.6	3.1
99	212	32	0.20	7.7	1.6	51.6	1.61E-04	1.4	44.8	3.0
100	214	31	0.20	7.8	1.6	48.6	1.59E-04	1.4	42.2	3.0
101	216	59	0.20	7.8	1.6	91.8	1.83E-04	1.6	93.3	3.2
102	218	20	0.20	7.9	1.5	30.1	2.26E-04	2.0	38.4	3.5
103	220	20	0.20	8.0	1.5	29.9	1.70E-04	1.5	29.0	3.0
104	222	20	0.20	8.0	1.5	29.7	1.59E-04	1.4	27.4	2.9
105	224	20	0.20	8.1	1.5	29.5	1.56E-04	1.4	27.0	2.8
106	226	20	0.20	8.1	1.5	29.3	1.54E-04	1.3	26.9	2.8
107	228	20	0.20	8.2	1.4	29.1	1.52E-04	1.3	26.7	2.8
108	230	20	0.20	8.2	1.4	28.9	1.47E-04	1.3	25.9	2.7
109	232	21	0.20	8.3	1.4	28.8	1.46E-04	1.3	26.1	2.7
110	234	21	0.20	8.3	1.4	28.6	1.43E-04	1.2	25.7	2.6
111	236	21	0.20	8.4	1.4	28.3	1.40E-04	1.2	25.4	2.6

112	238	21	0.20	8.5	1.3	28.1	1.40E-04	1.2	25.5	2.6
113	240	21	0.20	8.5	1.3	28.0	1.35E-04	1.2	24.8	2.5
114	242	21	0.20	8.6	1.3	27.8	1.36E-04	1.2	25.0	2.5
115	244	21	0.20	8.6	1.3	27.6	1.31E-04	1.1	24.2	2.4
116	246	22	0.20	8.7	1.3	27.6	1.29E-04	1.1	24.1	2.4
117	248	22	0.20	8.7	1.3	27.4	1.28E-04	1.1	24.0	2.4
118	250	22	0.20	8.8	1.3	27.2	1.27E-04	1.1	23.9	2.3
119	252	22	0.20	8.8	1.2	27.1	1.23E-04	1.1	23.4	2.3
120	254	22	0.20	8.9	1.2	26.9	1.22E-04	1.1	23.3	2.3
121	256	22	0.20	8.9	1.2	26.8	1.22E-04	1.1	23.4	2.3
122	258	22	0.20	9.0	1.2	26.7	1.18E-04	1.0	22.8	2.2
123	260	24	0.20	9.0	1.2	28.2	1.15E-04	1.0	23.8	2.2
124	262	49	0.20	9.1	1.2	57.6	1.15E-04	1.0	49.0	2.2
125	264	23	0.20	9.1	1.2	26.3	1.13E-04	1.0	22.2	2.1
126	266	23	0.20	9.2	1.1	26.0	1.12E-04	1.0	22.1	2.1
127	268	23	0.20	9.2	1.1	25.9	1.10E-04	1.0	21.9	2.1
128	270	23	0.20	9.3	1.1	25.7	1.08E-04	0.9	21.6	2.1
129	272	23	0.20	9.3	1.1	25.6	1.07E-04	0.9	21.4	2.0
130	274	23	0.20	9.4	1.1	25.5	1.06E-04	0.9	21.4	2.0
131	276	23	0.20	9.4	1.1	25.4	1.05E-04	0.9	21.4	2.0
132	278	24	0.20	9.5	1.1	25.2	1.02E-04	0.9	20.9	2.0
133	280	24	0.20	9.5	1.1	25.1	1.01E-04	0.9	20.7	1.9
134	282	24	0.20	9.6	1.1	25.0	9.89E-05	0.9	20.4	1.9
135	284	24	0.20	9.6	1.0	24.9	9.92E-05	0.9	20.6	1.9
136	286	24	0.20	9.7	1.0	24.8	9.75E-05	0.8	20.3	1.9
137	288	24	0.20	9.7	1.0	24.7	9.68E-05	0.8	20.3	1.9
138	290	24	0.20	9.7	1.0	24.6	9.67E-05	0.8	20.3	1.9
139	292	24	0.20	9.8	1.0	24.4	9.36E-05	0.8	19.8	1.8
140	294	24	0.20	9.8	1.0	24.3	9.35E-05	0.8	19.8	1.8
141	296	25	0.20	9.9	1.0	24.2	9.23E-05	0.8	19.7	1.8
142	298	25	0.20	10.0	1.0	23.5	9.19E-05	0.8	19.7	1.8
143	300	25	0.20	10.2	0.9	22.9	9.03E-05	0.8	19.5	1.7
144	302	47	0.20	10.4	0.9	41.7	8.98E-05	0.8	36.3	1.7
145	304	7	0.20	10.5	0.9	6.3	1.13E-03	9.8	71.1	10.7
146	306	6	0.95	10.3	0.0	0.3	2.67E-04	2.3	14.9	2.4
147	308	4	0.95	10.3	0.0	0.2	2.67E-04	2.3	9.3	2.4
1	310	69	0.95	10.3	0.0	2.7	1.19E-04	1.0	71.1	1.1
2	312	111	0.95	10.3	0.0	4.4	1.03E-04	0.9	99.3	0.9
3	314	124	0.95	10.3	0.0	4.9	1.07E-04	0.9	114.5	1.0
4	316	124	0.95	10.3	0.0	4.9	1.07E-04	0.9	114.9	1.0
5	318	124	0.95	10.3	0.0	4.9	1.08E-04	0.9	115.8	1.0

6	320	124	0.95	10.3	0.0	4.9	1.09E-04	0.9	116.8	1.0
7	322	124	0.95	10.3	0.0	4.9	1.10E-04	1.0	117.4	1.0
8	324	124	0.95	10.3	0.0	4.9	1.11E-04	1.0	118.8	1.0
9	326	124	0.95	10.3	0.0	4.9	1.11E-04	1.0	118.9	1.0
10	328	124	0.95	10.3	0.0	4.9	1.12E-04	1.0	120.1	1.0
11	330	124	0.95	10.3	0.0	4.9	1.14E-04	1.0	122.1	1.0
12	332	124	0.95	10.3	0.0	4.9	1.14E-04	1.0	122.5	1.0
13	334	124	0.95	10.3	0.0	4.9	1.16E-04	1.0	124.1	1.0
14	336	124	4.76	11.9	0.0	0.1	1.19E-04	1.0	127.2	1.0
15	338	124	4.76	16.3	0.0	0.1	1.26E-04	1.1	135.5	1.1
16	340	43	4.76	19.1	0.0	0.0	1.31E-04	1.1	49.2	1.1
23	DS Flange	1042	4.76	22.1	0.0	0.4	6.94E-05	0.6	627.6	0.6
22	End Flange	2797	4.76	25.1	0.0	0.8	6.11E-05	0.5	1482.1	0.5
	Bosses	364	4.76	27.1	0.0	0.1	6.11E-05	0.5	192.7	0.5
Total		**11173**				**8439**			**12558.8**	

Table I-b: Geometrical dimensions and heating loads of Horn1 outer conductor at steady state

MARS No	Z	Volume	Thickness	Mid-radius	Beam Heating		
	cm	cm^3	cm	cm	(GeV/cm^3-proton)	W/cm^3	W
10	0	1540	3.97	19.1	4.40E-05	0.4	585.2
1	0	314	0.26	16.2	6.06E-05	0.5	165.0
2	2	314	0.26	16.2	6.32E-05	0.5	172.5
3	4	314	0.26	16.2	6.69E-05	0.6	182.5
4	6	315	0.26	16.2	6.47E-05	0.6	176.6
5	8	315	0.26	16.2	6.53E-05	0.6	178.2
6	10	315	0.26	16.2	6.52E-05	0.6	178.1
7	12	314	0.26	16.2	6.51E-05	0.6	177.6
8	14	314	0.26	16.2	6.57E-05	0.6	179.1
9	16	314	0.26	16.2	6.46E-05	0.6	176.1
10	18	313	0.26	16.2	6.51E-05	0.6	176.9
11	20	314	0.26	16.2	6.41E-05	0.6	174.3
12	22	314	0.26	16.2	6.35E-05	0.6	173.0
13	24	313	0.26	16.2	6.34E-05	0.6	172.3
14	26	315	0.26	16.2	6.19E-05	0.5	169.2
15	28	314	0.26	16.2	6.23E-05	0.5	170.0
16	30	314	0.26	16.2	6.13E-05	0.5	167.1
17	32	314	0.26	16.2	6.10E-05	0.5	166.5
18	34	314	0.26	16.2	6.08E-05	0.5	165.7
19	36	314	0.26	16.2	6.01E-05	0.5	163.8
20	38	315	0.26	16.2	6.02E-05	0.5	164.4

21	40	314	0.26	16.2	5.97E-05	0.5	162.5
22	42	314	0.26	16.2	5.97E-05	0.5	162.4
23	44	315	0.26	16.2	5.93E-05	0.5	162.0
24	46	315	0.26	16.2	5.88E-05	0.5	160.7
25	48	313	0.26	16.2	5.92E-05	0.5	160.8
26	50	315	0.26	16.2	5.87E-05	0.5	160.2
27	52	314	0.26	16.2	5.88E-05	0.5	160.2
28	54	314	0.26	16.2	5.90E-05	0.5	160.6
29	56	315	0.26	16.2	5.86E-05	0.5	160.0
30	58	314	0.26	16.2	5.89E-05	0.5	160.6
31	60	315	0.26	16.2	5.86E-05	0.5	160.4
32	62	314	0.26	16.2	5.90E-05	0.5	160.7
33	64	314	0.26	16.2	5.89E-05	0.5	160.6
34	66	314	0.26	16.2	5.88E-05	0.5	160.4
35	68	314	0.26	16.2	5.89E-05	0.5	160.8
36	70	314	0.26	16.2	5.89E-05	0.5	160.5
37	72	314	0.26	16.2	6.04E-05	0.5	164.5
38	74	314	0.26	16.2	5.94E-05	0.5	161.8
39	76	315	0.26	16.2	5.98E-05	0.5	163.7
40	78	314	0.26	16.2	5.90E-05	0.5	160.9
41	80	314	0.26	16.2	5.88E-05	0.5	160.6
42	82	314	0.26	16.2	5.91E-05	0.5	160.9
43	84	314	0.26	16.2	5.89E-05	0.5	160.6
44	86	314	0.26	16.2	5.90E-05	0.5	161.0
45	88	314	0.26	16.2	5.90E-05	0.5	160.7
46	90	314	0.26	16.2	5.91E-05	0.5	160.9
47	92	314	0.26	16.2	5.91E-05	0.5	161.1
48	94	314	0.26	16.2	5.91E-05	0.5	161.1
49	96	314	0.26	16.2	5.92E-05	0.5	161.6
50	98	314	0.26	16.2	5.94E-05	0.5	161.7
51	100	313	0.26	16.2	5.96E-05	0.5	162.2
52	102	314	0.26	16.2	5.96E-05	0.5	162.5
53	104	314	0.26	16.2	5.97E-05	0.5	162.8
54	106	314	0.26	16.2	6.01E-05	0.5	163.8
55	108	314	0.26	16.2	6.01E-05	0.5	164.0
56	110	315	0.26	16.2	6.01E-05	0.5	164.4
57	112	314	0.26	16.2	6.04E-05	0.5	164.4
58	114	314	0.26	16.2	6.03E-05	0.5	164.4
59	116	315	0.26	16.2	6.04E-05	0.5	164.9
60	118	314	0.26	16.2	6.05E-05	0.5	164.9
61	120	315	0.26	16.2	6.05E-05	0.5	165.1

62	122	314	0.26	16.2	6.07E-05	0.5	165.3
63	124	314	0.26	16.2	6.07E-05	0.5	165.2
64	126	315	0.26	16.2	6.05E-05	0.5	165.3
65	128	314	0.26	16.2	6.07E-05	0.5	165.3
66	130	313	0.26	16.2	6.09E-05	0.5	165.5
67	132	314	0.26	16.2	6.07E-05	0.5	165.7
68	134	314	0.26	16.2	6.10E-05	0.5	166.0
69	136	314	0.26	16.2	6.10E-05	0.5	166.2
70	138	315	0.26	16.2	6.09E-05	0.5	166.4
71	140	314	0.26	16.2	6.10E-05	0.5	166.5
72	142	314	0.26	16.2	6.12E-05	0.5	166.9
73	144	314	0.26	16.2	6.13E-05	0.5	167.0
74	146	313	0.26	16.2	6.16E-05	0.5	167.5
75	148	314	0.26	16.2	6.14E-05	0.5	167.5
76	150	314	0.26	16.2	6.16E-05	0.5	168.0
77	152	314	0.26	16.2	6.17E-05	0.5	168.2
78	154	313	0.26	16.2	6.20E-05	0.5	168.6
79	156	314	0.26	16.2	6.19E-05	0.5	168.8
80	158	314	0.26	16.2	6.20E-05	0.5	169.3
81	160	314	0.26	16.2	6.22E-05	0.5	169.6
82	162	314	0.26	16.2	6.25E-05	0.5	170.1
83	164	314	0.26	16.2	6.27E-05	0.5	170.6
84	166	313	0.26	16.2	6.29E-05	0.5	171.2
85	168	314	0.26	16.2	6.29E-05	0.5	171.4
86	170	314	0.26	16.2	6.31E-05	0.5	172.0
87	172	314	0.26	16.2	6.32E-05	0.5	172.3
88	174	314	0.26	16.2	6.36E-05	0.6	172.9
89	176	314	0.26	16.2	6.37E-05	0.6	173.5
90	178	314	0.26	16.2	6.36E-05	0.6	173.4
91	180	315	0.26	16.2	6.37E-05	0.6	173.8
92	182	314	0.26	16.2	6.38E-05	0.6	174.0
93	184	314	0.26	16.2	6.38E-05	0.6	173.8
94	186	314	0.26	16.2	6.39E-05	0.6	174.0
95	188	315	0.26	16.2	6.38E-05	0.6	174.1
96	190	314	0.26	16.2	6.40E-05	0.6	174.5
97	192	314	0.26	16.2	6.39E-05	0.6	174.4
98	194	313	0.26	16.2	6.41E-05	0.6	174.3
99	196	314	0.26	16.2	6.39E-05	0.6	174.4
100	198	314	0.26	16.2	6.39E-05	0.6	174.2
101	200	314	0.26	16.2	6.38E-05	0.6	174.1
102	202	314	0.26	16.2	6.40E-05	0.6	174.5

103	204	314	0.26	16.2	6.40E-05	0.6	174.6
104	206	315	0.26	16.2	6.40E-05	0.6	174.6
105	208	313	0.26	16.2	6.42E-05	0.6	174.6
106	210	313	0.26	16.2	6.43E-05	0.6	174.7
107	212	314	0.26	16.2	6.41E-05	0.6	174.9
108	214	314	0.26	16.2	6.43E-05	0.6	174.9
109	216	314	0.26	16.2	6.41E-05	0.6	174.8
110	218	314	0.26	16.2	6.41E-05	0.6	174.8
111	220	314	0.26	16.2	6.41E-05	0.6	174.8
112	222	314	0.26	16.2	6.42E-05	0.6	174.8
113	224	314	0.26	16.2	6.42E-05	0.6	174.8
114	226	314	0.26	16.2	6.41E-05	0.6	175.0
115	228	315	0.26	16.2	6.41E-05	0.6	174.9
116	230	314	0.26	16.2	6.41E-05	0.6	174.9
117	232	316	0.26	16.2	6.37E-05	0.6	174.5
118	234	314	0.26	16.2	6.40E-05	0.6	174.5
119	236	314	0.26	16.2	6.40E-05	0.6	174.6
120	238	315	0.26	16.2	6.38E-05	0.6	174.0
121	240	314	0.26	16.2	6.38E-05	0.6	173.8
122	242	315	0.26	16.2	6.34E-05	0.6	173.5
123	244	314	0.26	16.2	6.35E-05	0.6	173.0
124	246	315	0.26	16.2	6.33E-05	0.5	173.0
125	248	314	0.26	16.2	6.34E-05	0.6	173.0
126	250	314	0.26	16.2	6.35E-05	0.6	173.0
127	252	314	0.26	16.2	6.34E-05	0.6	172.6
128	254	313	0.26	16.2	6.35E-05	0.6	172.7
129	256	315	0.26	16.2	6.32E-05	0.5	172.6
130	258	314	0.26	16.2	6.32E-05	0.5	172.4
131	260	314	0.26	16.2	6.33E-05	0.5	172.3
132	262	314	0.26	16.2	6.31E-05	0.5	172.0
133	264	314	0.26	16.2	6.29E-05	0.5	171.6
134	266	314	0.26	16.2	6.29E-05	0.5	171.3
135	268	314	0.26	16.2	6.28E-05	0.5	171.2
136	270	315	0.26	16.2	6.26E-05	0.5	171.1
137	272	314	0.26	16.2	6.27E-05	0.5	171.0
138	274	315	0.26	16.2	6.25E-05	0.5	170.6
139	276	315	0.26	16.2	6.24E-05	0.5	170.4
140	278	314	0.26	16.2	6.24E-05	0.5	170.2
141	280	314	0.26	16.2	6.23E-05	0.5	170.0
142	282	313	0.26	16.2	6.23E-05	0.5	169.5
143	284	314	0.26	16.2	6.23E-05	0.5	169.7

144	286	314	0.26	16.2	6.22E-05	0.5	169.5
145	290	315	0.26	16.2	6.20E-05	0.5	169.3
17	295	1725	0.26	16.2	4.15E-05	0.4	621.4
19	300	29	0.26	16.2	3.39E-05	0.3	8.4
20	305	29	0.26	16.2	3.39E-05	0.3	8.4
18	310	10779	0.26	16.2	4.15E-05	0.4	3882.0
21	315	2080	0.26	16.2	8.41E-05	0.7	1519.0
22	320	2797	0.48	16.2	6.11E-05	0.5	1482.1
Total		**64533**					**32603.4**